NK cells with tissue-resident traits shape response to immunotherapy by inducing adaptive anti-tumor immunity

Nicole Kirchhammer[1, 2*], Marcel P Trefny[1#], Marina Natoli[1#], Dominik Brücher[2, 3#], Sheena N Smith[2, 3], Franziska Werner[1, 4], Victoria Koch[1], David Schreiner[5], Ewelina Bartoszek[6], Mélanie Buchi[1], Markus Schmid[3, 7], Daniel Breu[3, 8], K Patricia Hartmann[3], Polina Zaytseva[3, 9], Daniela S Thommen[10], Heinz Läubli[11], Jan P Böttcher[12], Michal A Stanczak[1, 13], Abhishek S Kashyap[1, 14], Andreas Plückthun[3], Alfred Zippelius[1, 11]

[1] Cancer Immunology, Department of Biomedicine, University and University Hospital Basel, 4031 Basel, Switzerland

[2] Present address: Vector BioPharma AG, 4051 Basel, Switzerland

[3] Department of Biochemistry, University of Zurich, 8057 Zurich, Switzerland

[4] Present address: Molecular Dermato-Oncology and Tumor Immunology, Department of Dermatology, General Hospital Vienna, 1090 Vienna, Austria

[5] Immune Cell Biology, Department of Biomedicine, University Hospital Basel, 4031 Basel, Switzerland

[6] Microscopy Core Facility, Department of Biomedicine, University Hospital Basel, 4031 Basel, Switzerland

[7] Present address: Roche Diagnostics GmbH, 82377 Penzberg, Germany

[8] Present address: Department of Immunology, University Hospital Zurich, 8091 Zurich, Switzerland

[9] Present address: Institute for Regenerative Medicine, University of Zurich, 8952 Schlieren, Switzerland

[10] Division of Molecular Oncology and Immunology, The Netherlands Cancer Institute, 1066 Amsterdam, The Netherland

[11] Medical Oncology, University Hospital Basel, 4031 Basel, Switzerland

[12] Institute of Molecular Immunology and Experimental Oncology, Klinikum Rechts der Isar, School of Medicine, Technical University of Munich (TUM), 81675 Munich, Germany

[13] Present address: The Bloomberg-Kimmel Institute for Cancer Immunotherapy and Department of Oncology, Johns Hopkins University School of Medicine, Baltimore, MD 21287, USA

[14] Present address: Boehringer Ingelheim Pharmaceuticals, Inc., 6877 Ridgefield, USA

[*] Corresponding authors: Nicole Kirchhammer (nicole.kirchhammer@unibas.ch) and Alfred Zippelius (alfred.zippelius@usb.ch)

[#] Authors contributed equally

This manuscript has been accepted for publication in Science Translational Medicine, which is published by the American Association for Cancer Research. This is not the Version of Record and does not reflect post-acceptance improvements, or any corrections. The Version of Record is available online at https://doi.org/10.1126/scitranslmed.abm9043.

Abstract

T cell-directed cancer immunotherapy often fails to generate lasting tumor control. Harnessing additional effectors of the immune response against tumors may strengthen the clinical benefit of immunotherapies. Here, we demonstrate that therapeutic targeting of the IFNγ-IL-12 pathway relies on the ability of a population of NK cells with tissue-resident traits to orchestrate an anti-tumor microenvironment. Particularly, we utilized an engineered adenoviral platform as a tool for intra-tumoral IL-12 immunotherapy (AdV5-IL12) to generate adaptive anti-tumor immunity. Mechanistically, we demonstrate that AdV5-IL12 is capable to induce the expression of CCL5 in $CD49a^+$ NK cells both in tumor models and tumor specimens from patients with cancer. AdV5-IL12 imposed CCL5 induced cDC1 infiltration and thus increased DC-CD8 T cell interactions. A similar observation was made for other IFNγ-inducing therapies such as PD-1 blockade. Conversely, failure to respond to IL-12 and PD-1 blockade in tumor models with low $CD49a^+$ $CXCR6^+$ NK cell infiltration could be overcome by intra-tumoral delivery of CCL5. Thus, therapeutic efficacy depends on the abundance of NK cells with tissue-resident traits and specifically their capacity to produce the DC-chemoattractant CCL5. Our findings reveal a barrier for T cell-focused therapies and offer mechanistic insights into how T cell-NK cell-DC crosstalk can be enhanced to promote anti-tumor immunity and overcome resistance.

One sentence summary

A population of CCL5-producing NK cells with tissue-resident traits enhance T cell-DC crosstalk for successful cancer IL-12 immunotherapy.

Introduction

The clinical success of immune checkpoint blockade has initially kept the scientific focus predominantly on factors regulating T cell activity *(1)*. It is, however, increasingly acknowledged that a diverse range of immune cells, including components of innate immunity, must function in a coordinated and synergistic manner to successfully achieve immune-mediated tumor rejection *(2–4)*.

The interferon γ (IFNγ)- Interleukin 12 (IL-12) axis plays a central role in connecting innate and adaptive cancer immunity *(5)*. Mainly produced by dendritic cells (DCs) in the tumor microenvironment, IL-12 stimulates cytotoxicity and cytokine-secretion in T cells and natural killer cells (NK cells) *(6)*. In a positive IL-12-IFNγ feedback loop, T and NK cell-derived IFNγ in turn activates and induces IL-12 expression in DCs. Moreover, IFNγ enhances antigen cross-presentation by antigen-presenting cells (APCs) thereby further potentiating the cytotoxic activity of CD8 T cells *(5, 7)*. Consequently, gene expression signatures reflecting cellular components of this axis — NK cells, DCs, and CD8 T cells —, as well as signatures of IFNγ signaling are predictive of improved patient survival in multiple cancer types *(8–12)*. Furthermore, it has been shown that IL-12 induction by IFNγ is essential for the efficacy of immune checkpoint blockade *(5)*.

IL-12 has been extensively investigated for its use in cancer immunotherapy and has demonstrated remarkable antitumor efficacy in tumor models. However, in early clinical trials, its therapeutic benefit in patients remained limited with severe dose-limiting toxicity *(13, 14)*. A possible explanation is a lack of targeting to the tumor microenvironment. Most cytokines, including IL-12, act locally in the tumor and nearby lymph nodes in a paracrine or autocrine fashion, rather than systemically *(15)*. Although multiple approaches using localized IL-12 delivery are currently under investigation, the anti-tumor efficacy of local IL-12 therapy observed in mice has yet to be replicated in humans *(16–19)*.

We here sought to gain a deeper understanding of how IL-12-mediated tumor control is achieved and whether this knowledge ultimately allows to design improved treatment strategies for efficient tumor control. To this end, we utilized a tumor-targeted adenovirus serotype 5 delivery platform as a tool for intra-tumoral IL-12 immunotherapy (AdV5-IL12) *(20–22)*. In tumor models and patient-derived model systems, we demonstrate that the efficacy of IL-12 depends on the intra-tumoral abundance of a population of CD49a$^+$ NK cells with tissue-resident traits and their ability to prime the immune microenvironment by producing the chemokine CCL5. In CD49a$^+$ CXCR6$^+$ NK cell^{poor} tumors, resistance to IL-12 can be rescued by induced expression of CCL5, leading to increased infiltration of cDC1s, which then set the positive anti-tumor DC-T cell feedback loop in motion. Similarly, resistance to other IFNγ-mediated treatments such as PD-1 checkpoint blockade can be a result of reduced CCL5 induction due to a lack of CD49a$^+$ CXCR6$^+$ NK cells and can be overcome by treatment with CCL5. Our data highlight the importance of NK cells with tissue-resident traits for the induction of DC-T cell crosstalk and successful cancer immunotherapy.

Results

IL-12 immunotherapy prompts NK cells to orchestrate an anti-tumor microenvironment

Even though strategies to maximize IL-12 delivery are of increasing clinical interest, the therapeutic benefit in patients remains moderate. We first sought to identify cell types and key pathways underlying successful clinical outcomes to intra-tumoral IL-12 therapy in patients with melanoma (IL-12MEL trial; NCT01502293) *(16)*. To this end, we correlated tumor immune signatures derived from pre-treatment tumor biopsies with therapeutic responses. Patients with clinical responses showed higher NK cell and CD8 T cell scores compared to patients with tumor progression whereas no correlation was found with scores of other immune cells (Fig. 1A and fig. S1A).

To define a model system for local IL-12 therapy that reflects these clinical findings, we utilized a non-replicative, shielded, and re-targeted adenovirus serotype 5 vector previously established in our laboratory *(20–22)*. For this study, HER2 was used as a model antigen to target the HER2-overexpressing syngeneic tumor cell lines B16-HER2 and EMT6-HER2. Due to the high abundance of pre-existing antibodies against AdV5 in humans, we made use of a shield based on a hexon-binding humanized single-chain variable fragment (scFv), fully covering the virion *(22)*. To confirm tumor-specific expression of our payload, luciferase-encoding virus (AdV5-Luciferase) was peritumorally injected into B16-HER2 and EMT6-HER2 bearing mice (fig. S1B). In both tumor models, the payload was exclusively expressed in the tumor for up to 10 days with a peak expression on day 1 (fig. S1C–E).

To evaluate the efficacy of AdV5 encoding IL-12 (AdV5-IL12), we peritumorally treated mice bearing orthotopic (intra-mammary; i.m.) EMT6-HER2 tumors with four injections of $1.5x10^8$ PFU retargeted and shielded AdV5-IL12 initiated at day 7 post tumor inoculation. Empty virus (AdV5-control) served as a control (Fig. 1B). Treatment with AdV5-IL12 resulted in inhibition of tumor growth, enhanced survival, and complete tumor regression in 70% of treated mice; AdV5-control showed only moderate effects (Fig. 1C–D). No IL-12 was detected in the serum, confirming the specificity of our tumor-localized therapy (fig. S1F). Retargeted and shielded AdV5-IL12 showed increased efficacy compared to naked and retargeted vectors (fig. S1G).

As patients with localized IL-12 therapy show clinical responses even in non-treated lesions, we assessed the systemic effects of AdV5-IL12 in our mouse tumor model. To this end, we injected HER2-negative EMT6 wt cells into the contralateral flanks of the EMT6-HER2 tumor-bearing mice (fig. S1H). We observed reduced tumor growth of the contralateral tumors and complete regression in 50% of the AdV5-IL12 treated animals. This indicates systemic immune effects upon local administration of AdV5-IL12.

AdV5-IL12 induced the formation of protective anti-tumor immunological memory as mice that survived primary EMT6-HER2 engraftment following AdV5-IL12 treatment remained tumor-free after later re-challenge with the same cell line 80 days after first tumor cell inoculation (fig. S1I). Tumors from mice simultaneously inoculated with EMT6 wt cells on the lateral flank were equally rejected suggesting broad memory formation against shared antigens expressed by EMT6 cells (fig. S1I).

To dissect the role of defined immune cell populations in mediating the therapeutic effect of AdV5-IL12, we performed antibody-mediated depletion studies (Fig. 1E). In agreement with the immune signature

analysis from the IL-12MEL trial (Fig. 1A), AdV5-IL12 required both CD8 T cells and NK cells for therapeutic efficacy. As IL-12 is a known driver of IFNγ production in both those cell types and the clinical response correlates with a defined IFNγ score *(16)*, we assessed the contribution of IFNγ to the activity of AdV5-IL12. IFNγ-neutralized mice failed to control EMT6-HER2 tumors upon treatment with AdV5-IL12 (fig. S1J). In line with these findings, AdV5-IL12 increased the capacity of CD8 T cells and NK cells to proliferate and to exert effector functions as assessed by flow cytometry (fig. S2 and S3). In conclusion, mirroring the clinical situation, AdV5-IL12 treatment in EMT6-HER2 tumors requires robust NK and CD8 T cell responses which depend on IFNγ.

We next assessed the capability of CD8 and NK cells to directly interact and attack cancer cells using a highly multiplexed cytometric imaging approach, termed co-detection by indexing (CODEX) *(23)*. AdV5-IL12 led to a pronounced accumulation of CD45+ immune cells (fig. S4A–B). Spatial proximity (defined as a distance of <50 µm) of NK and CD8 T cells with tumor cells was specifically increased upon AdV5-IL12 treatment (Fig. 1F and fig. S4C). To confirm functional interactions and tumor lysis by NK and CD8 T cells, we analyzed the expression of the effector marker granzyme B in cells with spatial proximity to tumor cells (CD45- CD31-). In both NK and CD8 T cells, the number of granzyme B+ cells was increased in close proximity to tumor cells (Fig. 1G). In addition, the spatial proximity of CD8 T cells with DCs was specifically enhanced after AdV5-IL12 treatment (Fig. 1F). Moreover, the co-stimulatory molecules CD40, CD80 and MHCII, as well as PD-L1 on DCs in close proximity to CD8 T cells were specifically increased after AdV5-IL12 treatment, indicating an enhanced functional interaction between DCs and CD8 T cells induced by IL-12 (Fig. 1H). We also noticed close proximity of CD8 and NK to endothelial cells after AdV5-IL12 treatment (Fig. 1F and I) which may indicate induced trafficking of these cells by IL-12.

To investigate IL-12 induced immune cell recruitment to the tumor, we blocked lymphocyte recirculation with the trafficking inhibitor FTY720 *(24)*. FTY720 treatment prior to tumor inoculation fully abrogated tumor control. Blocking trafficking during AdV5-IL12 treatment allowed initial tumor control, but did not result in complete tumor regression (fig. S4D). This suggests that efficacious IL-12 responses require both pre-existing and actively recruited tumor infiltrating lymphocytes.

In addition to direct cytotoxicity against tumor cells, NK cells were shown to drive immune cell infiltration and intrinsic inflammation within tumors *(2, 9)*. To dissect the impact of NK cells on IL-12-induced recruitment, we depleted NK cells throughout the AdV5-IL12 treatment and assessed fate and infiltration of tumor-infiltrating immune cells (Fig. 1J and fig. S3). NK cell depletion led to a reduced number of MHCII+ CD103+ type I conventional dendritic cells (cDC1s, CD11c+ F4/80-; Fig. 1K). Furthermore, NK depletion was associated with reduced granzyme B expression in CD8 T cells, suggesting an important role of NK cells in facilitating optimal anti-tumor CD8 T cells responses (Fig. 1L). The number of macrophages (CD11b+ F4/80+) in the tumor was unchanged, however, depletion of NK cells skewed the polarization towards an immunosuppressive M2 (CD206+ MHCII-) phenotype (Fig. 1M). Thus, we concluded that during AdV5-IL12 treatment, NK cells orchestrate the recruitment and priming of essential cell subsets including cDC1s, and activated CD8 T cells to enhance tumor killing.

CCL5, mainly produced by CD49a$^+$ CXCR6$^+$ NK cells, is required for IL-12 mediated tumor rejection

To identify clinically relevant chemokines which may guide immune cell recruitment by NK cells after IL-12 therapy, we correlated NK cell scores with the expression of chemokines and their receptors in patients responding to IL-12 therapy (Fig. 2A). We identified that *CCL5* and its receptor *CCR5* strongly correlated with an NK score (Fig. 2B). Accordingly, *CCL5* was upregulated in patients with clinical responses (Fig. 2C). These results suggest that NK cells, likely through CCL5, are important in facilitating clinical responses to IL-12.

We therefore investigated whether NK cell-mediated CCL5 contributes to the efficacy of AdV5-IL12 in EMT6-HER2 tumors (i.m.). In line with the observed CCL5 upregulation in responding patients (Fig. 2C), AdV5-IL12 treatment of EMT6-HER2 tumors induced CCL5 expression in tumor lysates (Fig. 2D). CCL5 concentrations were reduced in tumor lysates after NK cell depletion, which confirms that in this model NK cells are the main source of CCL5 induced by AdV5-IL12 (Fig. 2D). Neutralizing CCL5 before tumor inoculation fully abrogated IL-12 efficacy; CCL5 neutralization after tumor inoculation but before AdV5-IL12 treatment partially inhibited IL-12 efficacy (Fig. 2E). Therefore, we concluded that CCL5 produced by NK cells plays a dual role in the response to IL-12 delivery. CCL5 at the steady-state permits responsiveness to AdV5-IL12 treatment, and further induction of CCL5 by AdV5-IL12 treatment may attract immune cells to improve anti-tumor immunity.

To analyze the contribution of CCL5 to NK cell-mediated tumor rejection upon AdV5-IL12 treatment, NK-depleted tumor-bearing mice were concomitantly treated with AdV5-IL12 and an AdV5 encoding CCL5 (AdV5-CCL5). While depletion of NK cells abrogated the efficacy of AdV5-IL12, the combination of AdV5-CCL5 with AdV5-IL12 partly rescued its efficacy (fig. S4E).

Recent studies have revealed that NK cells are highly heterogeneous with different immune functions *(25–27)*. To identify which NK cell subset produced CCL5, we analyzed CCL5 expression after AdV5-IL12 treatment in subpopulations of NK cells reflecting different maturation stages and subtypes, defined by CD11b and CD27 expression and by markers associated with homing or tissue-residency *(28, 29)*. We observed a higher proportion of NK cells associated with tissue-residency (CXCR6+ and CD49a+, CD11b-) producing CCL5 compared to mature (CD11b+) CXCR6 and CD49a low conventional NK (cNK) cells (Fig. 2F). Those CCL5-producing NK cells were also characterized by a high expression of CD27 (non-mature) and CD69 (associated with tissue-residency), and showed a low expression of CD62L which facilitates homing to secondary lymphatic tissues (fig. S4F). These findings suggest that responsiveness to IL-12 depends on CCL5-producing NK cells which exhibit features associated with tissue-residency with low maturation profile.

AdV5-CCL5 overcomes AdV5-IL12 resistance in CD49a$^+$ CXCR6$^+$ NK cell poor tumors

As CD49a$^+$ CXCR6$^+$ NK cell derived CCL5 was associated with treatment efficacy, we hypothesized that tumors with a lower proportion of this NK cell subpopulation would be largely resistant to AdV5-IL12 and could benefit from CCL5 supplementation. To test this and to exclude tumor cell-intrinsic resistance mechanisms, we injected EMT6-HER2 cells subcutaneously (s.c.), where we observed a lower amount of

CD49a$^+$ CXCR6$^+$ NK cells (Fig. 3A) while a similar number of cNK cells was assessed (Fig. 3B). Treatment of subcutaneous EMT6-HER2 tumors (CD49a$^+$ CXCR6$^+$ NK cell^{poor} TME) with AdV5-IL12 did not lead to a significant tumor reduction (fig. S5A) in contrast to intra-mammary-injected tumors (Fig. 1C and fig. S5B). However, we could observe an improved outcome when combining AdV5-IL12 treatment with AdV5-CCL5 in this setting (fig. S5A), confirming our hypothesis that a lack of CD49a$^+$ CXCR6$^+$ NK cells can be at least partialy rescued by CCL5 supplementation. To exclude a more general, NK cell-unrelated benefit of CCL5 supplementation, we treated mice bearing EMT6-HER2 tumor i.m. (CD49a$^+$ CXCR6$^+$ NK cell^{rich} TME) with the combination of both viral vectors which did not lead to an improved tumor control (fig. S5B).

To strengthen our conclusion, we utilized subcutaneous B16-HER2 as an orthotopic tumor model, which showed a low proportion of CD49a$^+$ CXCR6$^+$ NK cells but a similar number of cNK cells compared to the i.m. EMT6-HER2 model (Fig. 3A–B). In line with our findings that CD49a$^+$ CXCR6$^+$ NK cells are the major source of CCL5, the amount of CCL5 was not increased after AdV5-IL12 treatment in B16-HER2 tumors (Fig. 3C) in contrast to i.m. EMT6-HER2 tumors (Fig. 2D). Unlike in i.m. EMT6-HER2 tumors, NK cell depletion in B16-HER2 tumors did not increase tumor growth of untreated or AdV5-IL12 treated tumors, which supports our hypothesis that mainly NK cells with tissue-resident traits but not mature cNK cells determine IL-12 responsiveness (Fig. 1E and 3D).

We then asked if therapeutic CCL5 delivery using AdV5-CCL5 may compensate for the lack of CD49a$^+$ CXCR6$^+$ NK cells when combined with AdV5-IL12 in B16-HER2 bearing mice (Fig. 3E). Indeed, the combination further increased survival compared to AdV5-IL12 alone. We further confirmed our finding in mice bearing s.c. MC-38 tumors with low amounts of CD49a$^+$ CXCR6$^+$ NK cells comparable with B16-HER2 tumors (Fig. 3A). Therefore, we utilized shielded vectors without re-targeting to allow intrinsic transduction mechanisms. The combination of AdV5-IL12 with AdV5-CCL5 led to full tumor rejection in 50% of treated mice. Mice treated with AdV5-IL12 alone did not reject any tumors (fig. S5C).

To define factors that could explain the lack of efficacy of IL-12 in CD49a$^+$ CXCR6$^+$ NK cell^{poor} tumors, we compared which cell interactions were induced after IL-12 therapy in the B16-HER2 compared to the EMT6-HER2 mouse tumor model (Fig. 3F and fig. S6A–B). We observed two major differences in the changes to the interactome in B16-HER2 tumors. We noticed lower induction of NK-tumor and CD8 T-tumor, and lower induction of DC-CD8 T cell interactions by IL12 in the CD49a$^+$ CXCR6$^+$ NK cell^{poor} tumor microenvironment. Thus, CD49a$^+$ CXCR6$^+$ NK cell^{poor} B16-HER2 tumors are characterized by a reduced tumor attack of effector cells, and reduced induction of DC-CD8 T cell crosstalk by IL-12. Next, we asked whether CCL5 supplementation in CD49a$^+$ CXCR6$^+$ NK cell^{poor} B16-HER2 tumors could induce DC-CD8 T cell crosstalk and therefore promote anti-tumor T cell immunity. Utilizing multicolor flow cytometry, we were able to detect increased numbers of cDC1s when tumors were treated with either AdV5-CCL5 alone or in combination with AdV5-IL12 (Fig. 3G). Accordingly, we found an increased number of cDC1s expressing CD80 and PD-L1 in the AdV5-CCL5-AdV5-IL12 combination (Fig. 3H and fig. S6B–C), which indeed led to more interactions between DCs and CD8 T cells (Fig. 3I). In agreement, we observed more activated CD8 T cells in proximity to DCs (Fig. 3J) and an increased proportion of GzmB+ CD8 T cells (Fig. 3K). In addition, we could observe an increased number of interactions between DCs and tumor cells (fig.

S6C). To further understand the contribution of DCs to the therapeutic efficacy of the AdV5-IL12 + AdV5-CCL5 combination, we used Batf3 KO mice, lacking cDC1s *(30)*. The beneficial effect of AdV5-IL12 +/- AdV5-CCL5 on tumor control and survival was lost in Batf3 KO mice (Fig. 3L). Taken together, these data suggest that cDC1s attracted by CCL5 are essential for IL-12-mediated therapeutic benefit by enhancing T cell-mediated immunity; CCL5 can be provided by endogenous NK cells or therapeutically supplemented in a CD49a^{+} CXCR6^{+} NK cell^{poor} environment.

To show the potential of our adenoviral vector as a platform for combinatorial approaches, we then designed adenoviral vectors expressing both, IL-12 and CCL5 (fig. S6D). To avoid deletion of IL-12 or CCL5 by homologous recombination, we encoded both transgenes under the control of orthogonal promotors, cytomegalovirus- (CMV) or simian-virus 40- (SV40) promoter. We were able to demonstrate similar therapeutic efficacy by expressing both payloads within one viral vector, independent of the choice of the promotor, even though we thereby decreased the total viral load per injection (fig. S6E–F).

AdV5-huIL-12 induces CCL5 expression in CD49a^{+} CD16^{-} NK cells in patient-derived tumor cultures

To test whether a human IL-12-encoding HER2-targeted and shielded adenoviral vector (AdV5-huIL12) can induce similar anti-tumor effects in a human ex vivo system, we co-cultured primary tumor suspensions from patients with non-small cell lung cancer (NSCLC) (Fig. 4A) with a HER2-expressing ovarian cancer cell line (OVCAR3), which was transduced with AdV5-huIL12 (Fig. 4A–E). This experimental system has been shown to activate primary human lymphocyte subsets and trigger human cancer cell killing in response to PD-1/PD-L1 blockade *(31)*. Within patient-derived tumor-infiltrating lymphocytes (TILs) and OVCAR3 co-cultures, AdV5-huIL12 reduced OVCAR3 viability due to enhanced tumor cell killing (Fig. 4B). This effect was accompanied by an increase in IFNγ secretion (Fig. 4C) and induction of IFNγ-expressing patient-derived CD8 T cells and NK cells (Fig. 4D). In line with our murine data, CCL5 was upregulated in NK cells by IL-12, which we confirmed by depletion of NK cells in the co-culture system (Fig. 4E).

Next, we assessed the activity of AdV5-huIL12 using a human patient-derived tumor fragment model that preserves the tumor microenvironment and architecture but enables ex vivo perturbation by checkpoint blockade *(32)*. Tumor fragments of HER2-expressing ovarian cancer samples embedded in Matrigel (Fig. 4F and fig. S7A) were transduced with AdV5-huIL12. In all four tested patients, we noticed increased staining for IFNγ in CD8 T cells and CCL5 in NK cells (fig. S7B), the latter was confirmed in the supernatant by ELISA (Fig. 4G).

The identification of NK cells with tissue-resident traits as the main producers of CCL5 in the murine tumor models above prompted us to characterize which human tumor-infiltrating NK cells are producing CCL5. We therefore investigated the heterogeneity of tumor-infiltrating NK cells in patients with NSCLC using a published single-cell RNA sequencing (scRNASeq) data set *(33)*. We identified two main NK cell subsets with distinct gene expression profiles with the NK2 subcluster showing a higher expression of *CCL5* compared to the NK1 subcluster (Fig. 4H–I and fig. S8A–B). Recently, NK core signature genes associated with cytokine-producing phenotype (CD56^{bright} CD16^{-}) or tissue-residency have been described *(34, 35)*. We noticed a enrichment of CD56^{bright} CD16^{-} and tissue-residency genes in the CCL5-enriched NK2

subcluster (Fig. 4J). Core tissue-residency signature genes included upregulation of the integrin *ITGA1* (CD49a), *ITGAE* (CD103), *CD69*, and *ENTPD1* (CD39) which distinguishes NK2 from the highly *FCGR3A* (CD16)-expressing NK1 subtype (fig. S8C–F). To investigate whether IL-12 induces CCL5 production in NK cells with tissue-residency characteristics ($CD49a^+$ $CD16^-$), we characterized human tumor-infiltrating NK cells producing CCL5 in our co-culturing system (Fig. 4A and fig. S8). In line with our findings from mouse tumor models, $CD49a^+$ $CD16^-$ NK cells were producing higher amounts of CCL5 in response to AdV5-huIL12 compared to $CD16^+$ $CD56^{dim}$ conventional NK (cNK) cells (Fig. 4M). Collectively, these experiments recapitulate our finding that IL-12 can directly stimulate the antitumor activity of tumor-infiltrating T cells and induce CCL5 upregulation in NK cells with tissue-resident traits in primary human tumors.

CCL5 expression by NK cells with tissue-resident traits enhances the efficacy of PD-1 blockade

It has been demonstrated that IL-12-producing DCs, activated by IFNγ-secreting CD8 T cells, are critical for successful responses to anti-PD-1 treatments *(5)*. This led us to investigate whether the DC attractant CCL5 is associated with efficient tumor responses to anti-PD-1 therapy.

In patients with melanoma undergoing nivolumab treatment *(36)*, we compared CCL5-induction during treatment between patients which were responding (R) and non-responding (NR) (Fig. 5A). *CCL5* upregulation was associated with clinical responses (Fig. 5B). Futhermore, we noticed a positive correlation between the NK2 signature and *CCL5* expression (Fig. 5C) *(9)*. We also found a positive correlation between the level of *CCL5* and cDC1s in patients with treated melanoma (Fig. 5D). These findings suggest that CCL5 may be produced by intra-tumoral NK cells in response to PD-1 blockade and subsequently might promote cDC1 recruitment, which is in accordance with our observation in tumor models after IL-12 treatment.

To further investigate this possibility, we utilized the patient-derived tumor fragment platform, which allowed us to dissect the early immunological response of human tumor tissue to PD-1 blockade *(37)*. We measured IFNγ and CCL5 in the supernatants of tumor fragments from patients with cancer exposed to anti-PD-1 (Fig. 5E). In line with the correlative analysis of clinical trial data (Fig. 5B), we found increased CCL5 secretion in responding tumor fragments (defined by increased IFNγ secretion) with anti-PD-1 blockade (Fig. 5 F–G).

We next co-cultured human TILs with OVCAR3 cells in combination with anti-PD-1 (Fig. 5H). Anti-PD-1 treatment resulted in high concentrations of IFNγ and CCL5 in the supernatants and enhanced killing of OVCAR3 cells (Fig. 5I–K). The proportion of CCL5+ cells was higher in the $CD49a^+$ $CD16^-$ NK cells compared to cNK cells in co-cultures exposed to anti-PD-1 (Fig. 5K), which confirms NK cells with tissue-resident traits as the main source of immunotherapy-induced CCL5.

To further underline the beneficial response of CCL5-producing, tissue-resident NK2 cells upon PD-1 blockade, we re-analyzed a scRNASeq data set of patients with melanoma treated with immune-checkpoint inhibitors (ICI) *(38)*. We calculated the ratio of NK2 versus NK1 signature scores for each NK

cell in as a surrogate for NK2 characteristics while controlling for NK cell abundancy. Indeed, we observed that the NK2 phenotype was enriched in patients showing clinical responses (Fig. 5L).

Finally, we asked whether CCL5 can further boost anti-PD-1 therapy in CD49a^{+} CXCR6^{+}NK cell^{poor} tumors. We combined anti-PD-1 therapy with the adenoviral vector encoding CCL5 in B16-HER2 bearing mice (Fig. 5M). Whereas AdV5-CCL5 single treatment did not show any therapeutic efficacy, we observed increased therapeutic effects when combined with anti-PD-1 treatment. Taken together, these data demonstrate that CCL5 production by NK cells is important for the response to PD-1 blockade and CCL5-supplementing therapies can enhance the efficacy of PD-1 blockade in CD49a^{+} CXCR6^{+}NK cell^{poor} tumors.

Discussion

Multimodal immunotherapy combinations that target diverse immune-tumor interactions have become a cornerstone in the therapeutic management of patients with different cancer types and are being extensively explored to maximize the clinical benefit of cancer immunotherapies *(39–42)*. Here, we identify the lack of NK cells with tissue-resident traits as an unrecognized barrier to treatment effectiveness of targeted IL-12 and anti-PD-1 therapy (fig. S9). We show that IL-12 enhanced anti-tumorigenic DC-CD8 T cell interactions which relied on CD49a^{+} CXCR6^{+} NK cell-specific induction of CCL5. In tumor models with a limited number of those NK cells and thus low CCL5 expression, only moderate IL-12 responses were observed. However, responses of CD49a^{+} CXCR6^{+} NK cell^{poor} tumors could be rescued by concomitant administration of a CCL5-encoding adenoviral vector which – after converting tumor cells into CCL5 production sites – induced cDC1 infiltration and thus increased DC-CD8 T cell interactions. Due to the unique role of cDC1s in the initiation of T cell responses, both de novo and upon anti-PD-1 checkpoint inhibition, we subsequently observed that CCL5 produced by NK cells drives the response to anti-PD-1 therapy, which can be delivered using the AdV5 platform. These findings could be utilized to improve immunotherapy by fine-tuning the crosstalk between lymphoid and myeloid immune compartments utilizing multimodal combination immunotherapies adjusted to the pre-existing tumor microenvironment of each patient.

Viral vectors have been shown to be a suitable tool for local immunotherapy, reducing the systemic spread of therapeutic agents and consequently avoiding systemic side effects *(43)*. Our adenoviral platform utilizes exogenously added retargeting adaptors consisting of designed ankyrin repeat proteins (DARPins) *(44)*. This strategy has unique advantages, compared to targeting by genetic modifications, including the large existing library of DARPins and the rapid selection of new DARPin adapters against any given surface protein *(45, 46)*. Here, we targeted the model tumor-antigen HER2 which is overexpressed in different cancer types *(47)*. To further broaden the clinical applicability, DARPins may be selected to specifically recognize targets on cells other than tumor cells, such as tumor-associated antigens on stromal cells *(48, 49)*. Recently, the development of high-capacity, helper-dependent AdVs has enabled the expression of transgenes of up to 36 kilobase pairs. This, in combination with the targeted and shielded strategy, has increased the potential of AdVs as an ideal vector for multimodal cancer immunotherapy *(21, 22)*. Previous work has shown that adenoviral vectors can act as a "self-adjuvants", allowing the stimulation of multiple innate immune signaling pathways such as toll-like receptors and the induction of type I interferons upon viral entry *(50–52)*. Whereas these effects may explain the effect of the empty AdV5-control in tumor delay, the improved anti-tumor immunity supports the potential advantage of adenoviral vectors compared to other gene delivery vectors *(53, 54)*.

A variety of factors and cell types in the tumor microenvironment underpin the clinical success of cancer immunotherapies, and untangling these complex interactions is critical to understand and improve therapeutic efficacy *(55)*. Although typically rare, dendritic cells play a key role in orchestrating anti-tumor immunity. Consequently, intra-tumoral presence of DCs and particularly the production of IL-12 has been associated with better survival in various cancer types and is positively correlated with clinical outcome to

anti-PD-1 therapy *(2)*. Therefore, IL-12 has been extensively investigated for use in cancer immunotherapy. We here demonstrate that IL-12, provided intra-tumorally by paracrine AdV5 delivery, is capable to bridge innate and adaptive immunity. As a consequence of IL-12 produced by tumor cells after treatment, CD8 T cells, increased their activation and cytotoxic potential as demonstrated in tumors from patients and in tumor models. In the latter, early tumor growth control is achieved by the steady-state of lymphocytes present within the tumor. Yet, to achieve long-term tumor rejection, lymphocyte- and antigen-trafficking to draining lymph nodes is needed. In agreement, we observed increased numbers of NK cells and CD8 T cells in close proximity to blood vessels which suggests enhanced trafficking from the periphery to the tumor. This may be induced by the observed CCL5 secretion by CD49a^{+} CXCR6^{+} NK cells or other IFNγ-induced chemokines such as CXCL9 and CXCL10. Moreover, the fact that cDC1s have been described as the main source of CXCL9 and CXCL10 *(56)* could subsequently explain the increased interactions between CD8 T cells and DCs, which have initially been attracted to the TME by CCL5. Consequently, we demonstrated that AdV5-IL12 not only improves lymphocyte homing and activation in the primary tumor but also promotes abscopal anti-tumor effects at distant tumor sides.

NK cells contribute to various immune functions during cancer initiation and progression. Investigations of NK cells have originally emphasized their cytotoxic potential, in particular in the context of tumor immunity. Mature potent cytolytic effector CD56^{dim}CD16^{high} cNK cells, rapidly secreting pro-inflammatory cytokines and cytotoxic mediators upon receptor-mediated activation, have therefore been considered as the main subpopulations mediating tumor immunity. Tissue-resident NKs (trNKs) in contrast show reduced cytotoxic potential although being specialized on cytokine production such as TNFα, GM-CSF and IL-2 secretion. They have been described to express increased amounts of inhibitory checkpoint receptors and were therefore rather associated with tissue homeostasis *(57)*. In the context of cancer, they are poorly characterized and controversially discussed. They have been associated with poor survival in human hepatocellular carcinoma, whereas on the other hand, they are also reported to join forces with cNK cells to control liver metastasis *(58, 59)*.

We here demonstrate that NK cells with tissue-resident traits and their expression of CCL5 were essential for the efficacy of AdV5-IL12 and furthermore correlated with response to anti-PD-1 in patients with melanoma. Even though we observed expression of CCL5 in cNK cells and CD49^{+} NK cells in the steady-state, CD49^{+} $^{-}$NK cells specifically upregulated CCL5 in response to AdV5-IL12 and anti-PD1 treatment in mice and human tumor specimens. Therefore, we uncovered a role of NK cells with tissue-resident traits in priming the tumor immune microenvironment by inducing DC-CD8 T cell interactions and provide direct evidence that the lack of intra-tumoral cDC1 recruitment by NK cell population represents a major barrier for T cell-based therapies.

Some controversy exists regarding the role of CCL5 in cancer. A number of studies suggest that CCL5 has potential tumor-promoting effects, either by directly affecting tumor growth *(60)*, fostering an immunosuppressive tumor microenvironment *(61)*, enhancing tumor cell migration *(62)*, or expanding cancer stem cells *(63)*. In contrast, other studies show delayed tumor growth and prolonged survival in mouse models with CCL5-expressing tumor cells, as well as a correlation between CCL5 expression and

a T cell-inflamed phenotype in patients with cancer *(64–66)*. In our models, AdV5-CCL5 did not exhibit any tumor-promoting effects but also failed to show therapeutic benefits as a monotherapy. In agreement with previous work *(9)*, AdV5-CCL5 treatment induced cDC1 recruitment. However, only the combination with AdV5-IL12, led to higher co-stimulatory potential and subsequently increased tumor-reactive T cells. This suggests that the anti-tumorigenic properties of CCL5 are likely context-dependent: in the presence of other anti-tumorigenic signals induced by IL-12 or anti-PD1 treatment - which are known to tip the balance to a pro-inflammatory environment - CCL5 may further boost these effects which then translates into improved responses as evidenced by our in vivo data and analysis of patient cohorts. Besides CCL5, XCL1 has been described to have similar capacities in recruiting cDC1s to the tumor bed while not being reported to have tumor-promoting capacities *(9)*. On this note, XCL1 might be an intuitive alternative payload to guide cDC1s into tumors to improve anti-tumor immunity.

Whereas our study provides a phenotypical descrtiption of a population of CCL5-expressing NK cells with tissue-resident traits, it does not resolve its origin, transcriptional regulation and particularly its tissue-retention. Futhermore, this here described NK cell population share phenotypic features with both, tissue-resident NK cells and type 1 lymphoid cells (ILC1s) *(67)*. Single cell transcriptomics of tumor-infiltrating innate cells has recently advanced our understanding by revealing broad transcriptional clusters with a fluent transition between both cell types instructed by the tumor microenvironment *(58, 69)*. It will be of considerable interest in future studies to investigate the transcriptional regulation and effector differentiation of innate lymphocytes in tumors including the here described CCL5-producing cells. This will be instrumental in defining their lineage relationship and further resolves whether distinct functions can be assigned to a certain subtype. Particularly in patients treated with immunotherapy, niche-dependent or tumor-derived factors need to be identified that mediate resistance by limiting the accumulation, differentiation, survival, and function of these cells within the tumor microenvironment. Such factors may serve as predictive markers for T cell-focused therapies and define the need for potential combinations with cDC1 attracting agents such as CCL5, which allows to improve the efficacy of IFNγ-inducing therapies including IL-12 and checkpoint inhibition in tumors.

Taken together, our data highlight the importance of NK cells with tissue-resident traits and their capability to induce T cell immunity by enhancing DC-T cell crosstalk in IFNγ inducing therapies and may inform combination strategies utilizing viral vector platforms as an approach to further potentiate this NK cell-DC-T cell crosstalk. Our data highlight a relevant tumor-eliminating positive feedback mechanism to be prioritized for clinical development, particularly in patients with immune-excluded and/or resistant tumors.

Materials and Methods

Study design

These experiments were designed to evaluate the efficacy and resistance mechanisms of local IL-12 therapy in solid tumors in mice. Specifically, experiments were focused to identify soluble factors and their producer cells in the TME which restrict IL-12 response to finally overcome resistance by additional production of those factors using the here described adenoviral platform. The immunocompetent murine studies were complemented by in vitro experiments using primary human tumor material to confirm findings in a human setting. We used flow cytometry, multi-parameter microscopy, ELISAs and in vivo depletion/neutralization studies to identify resistance mechanisms. The investigators were not blinded to the allocation of groups during experiments or subsequently during the analysis. Although statistical methods were not used to pre-determine sample size, sample sizes were chosen on the basis of estimates from pilot experiments and previously published results. Animals were randomized to treatment groups following tumor implantation based on tumor size (30-70 mm^3) at treatment start-point. For cellular assessments, lymph node contaminated tumor digests were excluded defined by a B cell proportion over 20% of all CD45+ alive cells. The n values and particular statistical methods are indicated in the figure legends and the “Statstical analysis” section.

Redesign of AdV5 shuttle vector

The pShuttle vector from the AdEasy Adenoviral Vector System (Agilent Technologies) was redesigned to allow for the rapid generation and exchange of modular expression cassettes encoding a variety of payloads *(70)*. The multiple cloning site (MCS) of the pShuttle vector was replaced with synthetic MCS modules, called MCS1 or MCS2, by Gibson Assembly (New England Biolabs). The synthetic MCS1 module contained, from 5’ to 3’, the CMV promoter, NheI restriction site, XhoI restriction site, and the polyA site from bovine growth hormone (BGH) as previously described *(20)*. The MCS2 module contained, from 5’ to 3’, the SV40 promoter, SpeI restriction site, SalI restriction site and the polyA site from SV40. MCS modules were synthesized by GeneArt (Life Technologies Europe BV) containing the N-terminal flanking DNA 5’- GAA TAA GAG GAA GTG AAA TCT GAA TAA TTT TGT GTT ACT CAT AGC GCG TAA -3,' and C-terminal flanking DNA 5’- TAA GGG TGG GAA AGA ATA TAT AAG GTG GGG GTC -3' for Gibson Assembly into pShuttle to generate the plasmids pShuttle-MCS1 or pShuttle-MCS2. Additionally, a plasmid called pShuttle-MCS1-MCS2 was constructed where both the MCS1 and MCS2 modules were inserted in tandem into the same pShuttle construct.

Construction of payload construct

Murine and human IL-12 constructs were generated from translated Genbank cDNA sequences for the IL-12B/p40 (NCBI Reference: BC103608.1 or BC074723.2, respectively) and IL-12A/p35 (NCBI Reference: BC146595.1 or BC104984.1, respectively) connected by a F2A peptide as previously described *(21)*. The murine CCL5 gene was generated from Uniprot sequence P30882. Cytokines included their native signal sequences, were codon-optimized for human or mouse expression, respectively, and synthesized by

GeneArt (Thermo Fisher Scientific). For reporter assays, a firefly luciferase reporter was synthesized from GenBank: BAL46512.1. Payload constructs were inserted into redesigned pShuttle vectors by Gibson assembly or standard ligation cloning to generate pShuttle-MCS1 including the payload. The pShuttle-MCS1 backbone (without payload) was used to generate the AdV5-control vector. In general, pShuttle-MCS1-IL12 (AdV5-IL12), pShuttle-MCS1-CCL5 (AdV5-CCL5), and pShuttle-MCS1-Luciferase (AdV5-Luc) were used to generate immunotherapeutic vectors. For the combinatorial approach optimization (fig. S7D–F), pShuttle-MCS2-CCL5 (AdV5-SV40-CCL5) and pShuttle-MCS2-IL12 (AdV5-SV40-IL12), pShuttle-MCS1-IL12-MCS2-CCL5 (AdV5-CMV-IL12-SV40-CCL5) and pShuttle-MCS1-CCL5-MCS2-IL12 (AdV5-CMV-CCL5-SV40-IL12) were used.

Virus production

The plasmid containing the adenoviral genome, pAdEasy-1, from the AdEasy Adenoviral Vector System (Agilent Technologies) was previously modified to include a mutation to the hypervariable loop 7 (HVR7) of the hexon, which prevents blood factor X binding to virions and thus reduces liver infection *(22)*. To generate viral constructs, the modified pAdEasy-1_HVR7 plasmid was co-transformed with the pShuttle-MCS variants listed above into recA-proficient E. coli BJ5183 cells, from which the desired recombinants, obtained by homologous recombination, could be isolated for virus production. Packaging and amplification of adenoviral particles was performed by Vector Biolabs and they were purified on two consecutive cesium chloride density gradients and provided directly in PBS with 5% glycerol.

Protein purification of adenoviral shield and retargeting adaptor

The human HER2 adenoviral retargeting adapter (G3_1D3nc_SHP1) was expressed and purified as previously described *(22, 44)*. Endotoxin was removed from purified adapters using the Endotrap HD Endotoxin Removal System (Hyglos GmbH) and adapters were stored at -80°C in endotoxin-free Dulbecco's PBS (Millipore TMS-012-A). The adenoviral shield was purified in Sf9 insect cells as previously described *(22)*.

Mice

C57BL/6 and Balb/c mice were bred in-house at University Hospital Basel, Switzerland. Batf3 KO (B6.129S(C)-Batf3<tm1Kmm>/J) mice were obtained from the Jackson laboratory, USA. Animals were housed under specific pathogen-free conditions. All animal experiments were performed in accordance with Swiss federal regulations. Sex-matched littermates at 8-12weeks of age at the start of experiments were used.

Tumor models

$0.5x10^6$ syngeneic murine B16 D5 melanoma cells expressing HER2 (kindly provided by Dr. L. Weiner, Georgetown University, Washington, DC) or MC-38 colon carcinoma cells suspended in phenol red-free DMEM (without additives) were injected subcutaneously into the right flank of C57BL/6 and Batf3KO mice.

EMT6 murine breast cancer cells expressing HER2 ($1x10^6$) were injected subcutaneously or into the mammary gland of female Balb/c mice *(71)*. Cell lines were tested for mycoplasma contamination before injection. Tumor volume was calculated according to the formula: D/2 x d x d, with D and d being the longest and shortest tumor diameter in mm, respectively.

Immunotherapy treatments

Tumor bearing mice, with a tumor size of approximately 30-70 mm^3, were treated with each $1.5x10^8$ PFU of HER2-targeted and shielded adenoviral vectors in 50 µl of PBS (peritumorally), and/or 12.5 mg/kg mouse anti-PD-1 (RPM1–14, BioXCell) or left untreated. For depletion studies, CD8 T cells were depleted by administering anti-CD8a (53-6.72, BioXCell) at 10mg/kg (i.p.) once per week. NK depletion was performed by administering anti-Asialo-GM1 (Poly21460, Biolegend) 50 µl (i.p.) in Balb/c mice or anti-NK1.1 (PK136, BioXCell) 10 mg/kg (i.p.) in C57BL/6 mice every 4-5 days. IFNγ neutralization was performed using anti-IFNγ antibody (XMG1.2, BioXcell) at 25 mg/kg in 200 µl PBS injected every 2-3 days. To neutralize CCL5, we injected 32 µg anti-CCL5 antibody (500-P118, Peprotech) in 200 µl PBS per mouse intraperitoneally. Depletion and neutralization schedules were started the day before immunotherapy treatment unless stated otherwise.

Bilateral tumor models

Balb/c mice were inoculated with $1x10^6$ EMT6-HER2 tumor cells (i.m.) in the right flank. Four days later, 0.25 mio EMT6 wt cells were injected into the contralateral site (i.m.). On days 7, 9, 11, and 13 post first tumor inoculation, EMT6-HER2 tumors were treated with each $1.5x10^8$ PFU of HER2-targeted and shielded adenoviral vector encoding IL-12 in 50 µl of PBS (peritumorally). Tumor volumes of contralateral (EMT6 wt) tumors were measured.

Tumor re-challenge

Long-term surviving mice from AdV5-IL12 therapy were re-challenged with EMT6 wt and EMT6-HER2 tumors in each flank 60 days after primary tumor rejection. EMT6 wt and EMT6-HER2 re-challenge doses were 0.25 mio cells and 1 mio cells, respectively. As a control, naive Balb/c mice were implanted alongside re-challenged mice.

FTY720 treatments

Mice were implanted with EMT6-HER2 or B16-HER2 tumors intramammary or subcutaneously, respectively. Mice were treated or not with 1.25 mg/kg of FTY720 (Cayman Chemical) i.p. daily throughout the duration of the experiment. Injections were started one day before tumor inoculation or the day before adenoviral treatment.

In vivo pharmacokinetic experiments

Mice were implanted with EMT6-HER2 or B16-HER2 tumors intramammarily or subcutaneously, respectively. Once the tumors reached an average volume of 30-70 mm^3, luciferase-encoding retargeted and shielded AdV5 ($1.5x10^8$ PFU per mouse; AdV5-Luc) were injected peritumorally. The luciferase signal was determined in live animals one day after virus injection and 10 minutes after intraperitoneal injection of 150 mg/kg D-luciferin (PerkinElmer) using the in vivo imaging system NightOWL II LB 983 (Berthold) over two weeks. Following live imaging, luciferase activity was determined in isolated tumors and organs (draining and non-draining lymph nodes, spleen, liver, kidney, lung, and heart). The overlay of the real image and the luminescence representation allowed the localization and measurement of luminescence emitted from xenografts. The signal intensities from manually derived regions of interest (ROI) were obtained and data were expressed as photon flux (photon/s). All measurements were performed under the same conditions, including camera settings, exposure time (60 s), distance from lenses to the animals and ROI size.

Multiparameter flow cytometry

Tumor tissue was isolated from mice, weighed, and minced using razor blades. Tissue was then digested using accutase (PAA), collagenase IV (Worthington), hyaluronidase (Sigma), and DNAse type IV (Sigma) for 60 min at 37°C with constant shaking. The cell suspensions were filtered using a cell strainer (70 µm). Precision Counting beads (Biolegend) were added before staining to quantify the number of cells per gram tumor. Single cell suspensions were blocked with rat anti-mouse FcγIII/II receptor (CD16/CD32) blocking antibodies ("Fc-Block") and stained with live/dead cell-exclusion dye (Zombie UV dye; Biolegend). The cells were then incubated with fluorophore-conjugated antibodies (Table 1) directed against cell surface antigens, washed, and resuspended in FACS buffer (PBS + 2% FBS). For intracellular/intranuclear antigens, cells stained with cell surface antibodies were fixed and permeabilized using Foxp3/transcription factor staining buffer set (eBioscience) prior to incubation with antibodies directed against intracellular antigens. Cell populations were analyzed on a Cytek Aurora and Cytoflex.

Bioinformatic analysis of flow cytometry data

FCS files containing pre-gated alive CD45+ single cells were read into R using the flowCore package (flowCore: flowCore: Basic structures for flow cytometry data version 2.2.0 from Bioconductor). A logicle transform was performed per channel, with parameters calculated from aggregated data from all samples. CD45 low cells with a transformed value of < 2.5 were removed from further analysis (threshold set on the left side of trough of density plot of transformed CD45 values from all samples). The measurements were randomly subsampled to 1.5×10^5 cells per condition to expedite downstream operations. Principal Component Analysis (PCA) was performed using all markers except for CD45, Live-Dead, FSC*, and SSC*. Uniform Manifold Approximation and Projection (UMAP) was performed for visualization using the CATALYST module's runDR function (CATALYST: Cytometry dATa anALYSis Tools version 1.14.0 from Bioconductor). Clustering was performed using Rphenograph (0.99.1), an R implementation of

PhenoGraph (GitHub - JinmiaoChenLab/Rphenograph: Rphenograph: R implementation of the PhenoGraph algorithm) *(75)*. Five clusters with universally high expression across all markers were removed, and steps starting with PCA were repeated. Three resulting clusters were again removed and the process iterated once more to yield the final clustering, UMAP, and heatmaps *(76)*. Supplemental UMAP visualization of scaled marker expression done with CATALYST's plotDR function. Main cell types were assigned by marker expression. To confirm certain assignments, cell populations were gated using FlowJo (10.6.2) and compared to assigned populations, such as NK cells: NKp46+, CD3-, CD19- Ly-6G-, F4/80-.

Multiparameter fluorescence microscopy

Tumors embedded in OCT were sectioned into 7 µm-thick slices and attached to poly-L-lysine coated square coverslips. Sections were analyzed using CODEX (Akoya Biosciences), a highly multiplexed imaging platform, which allows the staining of solid tissue sections with a panel of up to 40 antibodies at once *(23)*. In brief, CODEX uses a unique DNA barcode system to label each antibody clone individually. These barcodes can be detected by reversible hybridization to their corresponding reporter. The respective reporters, which are conjugated with the fluorophores AF488, Atto550, or Cy5, are applied onto the tissue sections, imaged, and removed in a multicycle experiment. For this purpose, the manufacturer's protocol "CODEX User Manual Rev A.0" (provided by AKOYA Biosciences) was followed.

The antibody panel was composed of commercially available AKOYA-conjugated antibodies and self-conjugated custom antibodies (CODEX Conjugation Kit, AKOYA Biosciences; Table 2). Tissue staining was performed with the CODEX Staining Kit (AKOYA Biosciences). Briefly, the tissue was thawed with drierite beads, fixed with acetone, rehydrated, and fixed with 1.6% paraformaldehyde (PFA). After blocking, the tissue was stained with the established antibody panel consisting of 33 barcoded antibodies at the same time. The bound antibodies were fixed to the tissue with 1.6% PFA, ice-cold methanol, and a fixative solution (AKOYA Biosciences).

The inverse microscope DMi8 (Leica) was used for acquisition (20x magnification, xyz acquisition mode 14 Z-stacks each 14.99 µm, "Best Focus" autofocus with default settings). The generated fluorescence data were formatted with the Akoya CodexDriver V2 and subsequently processed using CODEX Processor (Version v1.5.0.48b) or the Kheops PlugIn in ImageJ and QuPath0.2.3 and StarDist *(77–79)*. The processing steps included 1) XY Processing with tile registration and shading correction; 2) Z-Stack Processing with deconvolution, drift compensation, overlap cropping, background subtraction (min-min mode), and best focus detection; 3) Stitching with best focus interpolation and tile overlap of 10% and 4) Cell segmentation on the nuclear stain with the radius 8 or threshold (0.69), channels ('DAPI'), normalize percentiles (1.99), pixel size (0.423), cell Expansion (2.8), cell constrain scale (1.5) in StarDist, respectively. The processed and segmented data were analyzed with the CODEX Multiple Analysis Viewer (Version 1.2.0.297) or the PhenoGraph algorithm using R 4.0.2. Manual gating was performed to distinguish between CD45+ cells (immune cells) and CD45- cells (tumor and stroma cells). Clustering was performed with VORTEX using unbiased hierarchical X-shift clustering (K = 55 resulting in 81 immune clusters) *(80)*.

Clusters were manually verified and assigned to main immune cell populations using CODEX Multiple Analysis Viewer or QuPath. Subsequently, mean marker expression and interaction counts between cellular main populations (cells with <50 µm proximity) were determined.

Interaction analysis

Interaction counts between main cell populations (contact defined as <50 µm proximity) were used for further analysis. The cluster "L" containing lymph vessels was excluded from further analysis, because of the very distinct localization of its cells as small vessels. Expected interaction counts for each cell-cell interaction pair were calculated as:

$$\mathrm{expectedInteractions}_{\mathrm{CellA\_CellB}} = \mathrm{interactions}_{\mathrm{allCells}} * \mathrm{frequency}_{\mathrm{CellA}} * \mathrm{frequency}_{\mathrm{CellB}}$$

Next, a negative-binomial generalized linear model for the interaction counts with an offset of log(expectedInteractions) was generated in R 4.0.2. The mathematical interaction terms between cell-cell type comparison (DC_vs_CD8) and experimental condition (untreated, AdV5-empty, AdV5-IL12) were used to calculate odds ratios and p-values for changes in cell-cell type interactions between experimental conditions. Odds ratios for different subsets of immune cells were plotted using ggplot2.

Intra-tumoral and systemic cytokine measurements

Serum was collected in EDTA containing tubes (Sarstedt) and IL-12 levels were determined using the IL-12 p70 Mouse Uncoated ELISA Kit (Invitrogen). Isolated tumors were snap-frozen on dry ice. Before thawing, a 5 mm metal bead and 1 ml of lysis buffer (20 mM Tris HCl (pH 7.5), 0.5% Tween 20, 150 mM NaCl, Sigma protease inhibitors 1:100) were added to the tubes. Tumors were lysed using a TissueLyser (Qiagen) for 5 min at 25 Hz. After centrifugation, protein concentrations were determined with the Pierce BCA Protein Assay Kit (Thermo Scientific). CCL5 concentration in the tumor lysates was analyzed by ELISA (Mouse RANTES Uncoated ELISA Kit Invitrogen) and normalized to the determined total protein concentrations.

Patients and sample preparation

Surgical specimens were mechanically dissociated, digested with accutase (PAA Laboratories), collagenase IV (Worthington), hyaluronidase (MilliporeSigma), and DNAse type I (MilliporeSigma), filtered, washed, and frozen as single cell suspension for future use. For human ex vivo tumor cultures, surgical specimens were dissected into tumor fragments and frozen for future use. Human PBMCs were isolated by density gradient centrifugation using Histopaque-1077 (MilliporeSigma) from buffy coats obtained from healthy blood donors (Blood Bank, University Hospital Basel). PBMCs were frozen for later use in liquid nitrogen. For NK cell depleted co-cultures a positive selection using CD56 MicroBeads, an LS Column, and a MidiMACS™ Separator was performed (Milteny). Ethics approval was obtained from the local ethical committee to analyze the tissue and blood samples (Ethikkommission Nordwestschweiz) and written informed consent was obtained from all patients prior to sample collection.

Ex vivo human immune cells and tumor co-culture experiments

Healthy donor PBMCs or tumor digest samples, processed as described above, were co-cultured with OVCAR3 human ovarian cancer cell line, similarly to as described in Natoli et al. 2020. Briefly, 6000 OVCAR3 cells were seeded on the wells of a flat-bottom 96-well plate in RPMI containing L-glutamine (R8758, Sigma-Aldrich), supplemented with penicillin/streptomycin (100 ng/ml, Sigma-Aldrich) and 10% FBS (Sigma-Aldrich). After 2 hours, the medium was replaced with fully supplemented RPMI containing AdV5-hu-IL12 or empty vector control (AdV5-control) at a PFU of 1000/cell. Additional control wells were left untreated. After 2 hours of incubation, the medium was replaced to remove the virus and the tumor cells were incubated for 2 days at 37°C, 5% CO2. 300,000 healthy donor PBMCs or single cells from tumor digest samples were then added to the wells of the 96-well plate in a final volume of 200 µl per well. Tumor cell (OVCAR3) viability was assessed by an MTT assay and flow cytometry was conducted on the suspension cells (PBMCs, TILs) after 3 days of co-culture. The supernatant was collected after 6 days of co-culture to assess IFNγ and CCL5 production using a Human IFNγ ELISA Set (BD OptEIA, 555142) and ELISA MAX Deluxe Set Human CCL5 (Biolegend, 440804), respectively, according to the manufacturers' instructions.

Ex vivo tumor fragment culture

Tumor fragment cultures were prepared as described in Voabli et al. 2021. Briefly, frozen patient tumor fragments were slowly thawed at 37°C and extensively washed in PBS and warm RPMI medium containing L-glutamine (R8758, Sigma-Aldrich), supplemented with penicillin/streptomycin (100 ng/ml, Sigma-Aldrich), 10% FBS (Sigma-Aldrich), 1x MEM Non-Essential Amino Acids (Gibco) and 1 mM sodium pyruvate (Sigma-Aldrich).

Single tumor fragments were then embedded in a total of 80 µl of an artificial extracellular matrix within the wells of a flat-bottom 96-well plate. The extracellular matrix was prepared by mixing ice-cold sodium bicarbonate (Sigma; 1.1% final concentration), collagen I (Corning; 1 mg/ml final concentration) and fully supplemented RPMI with ice-cold matrigel (Matrix High Concentration, Phenol Red-Free, BD Biosciences; 4 mg/ml final concentration). 40 µl of matrix was solidified by incubation at 37°C for 20-30 min. One tumor fragment per well was placed on top of the pre-solidified matrix, after which a second layer of 40 µl matrix was added. Plates were then placed in a 37°C incubator for further 20-30 min. 110 µl of fully supplemented RPMI was added on top of the matrix. 1 mio PFU of AdV5-hu-IL12 or control AdV5-control or nivolumab (10 µg/ml final concentration) were added to each well containing individual tumor fragments. Between 6-12 fragments were used for each treatment conditions. After 48 hours of incubation at 37°C, the fragments were pooled and enzymatically digested and filtered into single cell suspensions, as described above. Flow cytometry was conducted and the supernatant was collected from each well to assess IFNγ and CCL5 concentrations using a Human IFNγ ELISA Set (BD OptEIA, 555142) and ELISA MAX Deluxe Set Human CCL5 (Biolegend, 440804), respectively, according to the manufacturers' instructions.

MTT assay

To assess tumor cell viability in co-culture experiments, an MTT assay was used as follows. The medium from the co-culture wells was removed and the wells were gently washed once with PBS to remove suspension cells. MTT (Sigma-Aldrich) was then added at 500 µg/ml and the tumor cells were incubated at 37°C for 2–3 hours. Formazan crystals were resuspended in 90 µl of dimethyl sulfoxide (DMSO; Sigma-Aldrich) and absorbance was measured at a wavelength of 570 nm.

Bioinformatic analysis of published gene expression data of human melanoma samples

We received the normalized Nanostring RNA expression data from the NCT01502293 trial (Oncosec), in which patients received IL-12-encoding mRNA by intra-tumoral electroporation *(16)*. The gene signatures for different immune sub-populations were retrieved from the PanCancerImmunology Nanostring panel. The transcripts within the "Cytotoxic cells" signature can't be attributed to a single cell type and are found in other signature lists of both NK and CD8 T cells. Therefore, its transcripts were merged with the cytotoxic NK and CD8 T cells resulting in the "CD8+ T cells" and "NK cells" signatures. Importantly, neither "CD8+ T cells" and "NK cells" contained the *CCL5* transcript. Downstream analysis of all Nanostring data was performed using R version 4.0.2 and visualized in GraphPad Prism 9.

Immune cell infiltration was estimated by calculating a signature score as described by Cursons et al. 2019. Briefly, all transcripts for each sample were ordered by decreasing expression and the signature score was defined as:

$$1 - \frac{\text{mean rank of signature transcripts}}{\text{number of all transcripts}}$$

Thus, a high signature score indicates enrichment of signature transcripts among genes with high expression. To find genes that correlate with the NK cells signature score, we performed a linear regression for signature scores with log-transformed transcript counts. p-values were adjusted by the Benjamini-Hochberg correction method.

We also reanalyzed RNAseq data of samples from patients with tumor treated with anti-PD-1 antibodies (nivolumab) *(36)*. Data was downloaded from the GEO under accession number GSE91061. Only patients with both pre- and post-treatment samples and evaluated responses were analyzed. Counts were normalized by library size using edgeR and displayed as log counts per million using GraphPad Prism 9. Paired two-way ANOVA with multiple comparisons and the post-hoc test were used to calculate significances for increased *CCL5* expression upon treatment in CB. The availability of RNAseq data allowed the use of more complex gene signatures than with Nanostring data above. Therefore, we used the signatures described by Tirosh et al and Cursons et al. for this analysis *(81, 82)*. As we wanted to correlate signatures with *CCL5* expression, *CCL5* was excluded from the T cell signature provided by Tirosh et al. 2016. Signature scores were calculated as described above.

For the reanalysis of the Zillionis et al. scRNAseq dataset we downloaded the pre-cleaned count matrix from GEO under accession number GSE127465. The dataset was analyzed using the Bioconductor packages SingleCellExperiment and scater. PCA was performed using the top 4000 variable gene log counts. UMAP dimension reduction was performed on the PCA values using the scater runUMAP with 15 neighbors. *CCL5* expression per cell was visualized by ggplot2 using UMAP coordinates. To construct the NK1 and NK2 signatures we extracted the z-scores for genes enriched in either cluster using the online tool of the original publication. We then selected genes with a z-score of >0.5 and a minimum difference in z-score between the two subsets of 0.5.
We also obtained signatures for tissue resident NK cells from Marquart et al and a signature for $CD56^{bright}$ $CD16^{neg}$ NK cells from Hanna et al *(34, 35)*. A score for each signature as above was then calculated for each cell in the Zillionis dataset. Violin plots of these values were then plotted using Graphpad Prism.

Similarly, we also obtained the scRNAseq dataset described in Sade-Feldmann et al. under GEO accession number GSE120575. As described in their original publication, genes were filtered for protein coding genes and min expression of >4.5 logcounts in at least 10 cells. Cells were filtered to have >2.5 mean logcounts of their listed housekeeping genes. Cells with a high fraction mitochondrial reads (>3 standard deviations; dying cells) and very many detected genes (> 4 standard deviations; doublets) were excluded. PCA and UMAP dimension reductions were calculated as above. Clustering was performed using buildSNNGraphs of the scran package from PCA values and k = 15. Cluster8 consisted of NK cells based on its high expression of *NCR1*, *NCAM*, and *FCGR3A*. For each cell in this NK cluster, we calculated the mean score for NK1 and NK2 signatures as described above. Then we summarized the mean NK1 and NK2 value for the NK cells of each patient. The values for responding and non-responding patients were then visualized as a ratio between NK2 and NK1 cells using Graphpad Prism.

Statistical analysis

For normally-distributed datasets, we used 2-tailed Student's t test and one-way ANOVA followed by Holm-Sidak multiple comparison test. When variables were not normally distributed, we performed non-parametric Mann-Whitney or Kruskal-Wallis tests. For survival analysis, *P* values were computed using the Log Rank test. Two-way ANOVA was used to compare tumor growth curves and grouped data sets. *P* values > 0.05 were considered not significant, *P* values < 0.05 were considered significant. * *P* value < 0.05, ** *P* value < 0.01, *** *P* value < 0.001, **** *P* value < 0.0001.

Supplementary Materials

Fig S1 to S9

Table S1 to

S2

Data File S1.

MDAR reproducibility sheet

References

1. A. D. Waldman, J. M. Fritz, M. J. Lenardo, A guide to cancer immunotherapy: from T cell basic science to clinical practice*Nature Reviews Immunology* **20**, 651–668 (2020).

2. K. C. Barry, J. Hsu, M. L. Broz, F. J. Cueto, M. Binnewies, A. J. Combes, A. E. Nelson, K. Loo, R. Kumar, M. D. Rosenblum, M. D. Alvarado, D. M. Wolf, D. Bogunovic, N. Bhardwaj, A. I. Daud, P. K. Ha, W. R. Ryan, J. L. Pollack, B. Samad, S. Asthana, V. Chan, M. F. Krummel, A natural killer–dendritic cell axis defines checkpoint therapy–responsive tumor microenvironments, *Nature Medicine* **24**, 1178–1191 (2018).

3. A. Gardner, Á. de Mingo Pulido, B. Ruffell, Dendritic Cells and Their Role in Immunotherapy, *Frontiers in Immunology* **11**, 1–14 (2020).

4. N. D. Huntington, J. Cursons, J. Rautela, The cancer–natural killer cell immunity cycle, *Nature Reviews Cancer* **20**, 437–454 (2020).

5. C. S. Garris, S. P. Arlauckas, R. H. Kohler, M. P. Trefny, S. Garren, C. Piot, C. Engblom, C. Pfirschke, M. Siwicki, J. Gungabeesoon, G. J. Freeman, S. E. Warren, S. F. Ong, E. Browning, C. G. Twitty, R. H. Pierce, M. H. Le, A. P. Algazi, A. I. Daud, S. I. Pai, A. Zippelius, R. Weissleder, M. J. Pittet, Successful Anti-PD-1 Cancer Immunotherapy Requires T Cell-Dendritic Cell Crosstalk Involving the Cytokines IFN-γ and IL-12, *Immunity* (2018), doi:10.1016/j.immuni.2018.09.024.

6. S. Tugues, S. H. Burkhard, I. Ohs, M. Vrohlings, K. Nussbaum, J. Vom Berg, P. Kulig, B. Becher, New insights into IL-12-mediated tumor suppression, *Cell Death and Differentiation* **22**, 237–246 (2015).

7. B. Ruffell, D. Chang-Strachan, V. Chan, A. Rosenbusch, C. M. T. Ho, N. Pryer, D. Daniel, E. S. Hwang, H. S. Rugo, L. M. Coussens, Macrophage IL-10 Blocks CD8+ T Cell-Dependent Responses to Chemotherapy by Suppressing IL-12 Expression in Intratumoral Dendritic Cells, *Cancer Cell* **26**, 623–637 (2014).

8. M. Ayers, J. Lunceford, M. Nebozhyn, E. Murphy, A. Loboda, D. R. Kaufman, A. Albright, J. D. Cheng, S. P. Kang, V. Shankaran, S. A. Piha-Paul, J. Yearley, T. Y. Seiwert, A. Ribas, T. K. McClanahan, IFN-γ-related mRNA profile predicts clinical response to PD-1 blockade, *Journal of Clinical Investigation* **127**, 2930–2940 (2017).

9. J. P. Böttcher, E. Bonavita, P. Chakravarty, H. Blees, M. Cabeza-Cabrerizo, S. Sammicheli, N. C. Rogers, E. Sahai, S. Zelenay, C. Reis e Sousa, NK Cells Stimulate Recruitment of cDC1 into the Tumor Microenvironment Promoting Cancer Immune Control, *Cell* **172**, 1022-1037.e14 (2018).

10. J. Cursons, A gene signature predicting natural killer cell infiltration and improved survival in melanoma patients, *Cancer Immunol. Res.* **7**, 1162–1174 (2019).

11. Y. Zhao, C. K. Lee, C. H. Lin, R. B. Gassen, X. Xu, Z. Huang, C. Xiao, C. Bonorino, L. F. Lu, J. D. Bui, E. Hui, PD-L1:CD80 Cis-Heterodimer Triggers the Co-stimulatory Receptor CD28 While Repressing the Inhibitory PD-1 and CTLA-4 Pathways, *Immunity* **51**, 1059-1073.e9 (2019).

12. H. Lee, Integrated molecular and immunophenotypic analysis of NK cells in anti-PD-1 treated metastatic melanoma patients, *Oncoimmunology* **8** (2019).

13. G. R. Weiss, M. A. O'Donnell, K. Loughlin, K. Zonno, R. J. Laliberte, M. L. Sherman, Phase 1 Study of the Intravesical Administration of Recombinant Human Interleukin-12 in Patients With Recurrent Superficial Transitional Cell Carcinoma of the Bladder, *Journal of Immunotherapy* **26**, 343–348 (2003).

14. J. A. Hurteau, J. A. Blessing, S. L. DeCesare, W. T. Creasman, Evaluation of recombinant human interleukin-12 in patients with recurrent or refractory ovarian cancer: A gynecologic oncology group study, *Gynecologic Oncology* **82**, 7–10 (2001).

15. K. G. Nguyen, M. R. Vrabel, S. M. Mantooth, J. J. Hopkins, E. S. Wagner, T. A. Gabaldon, D. A. Zaharoff, Localized Interleukin-12 for Cancer Immunotherapy, *Frontiers in Immunology* **11**, 1–36 (2020).

16. A. Algazi, S. Bhatia, S. Agarwala, M. Molina, K. Lewis, M. Faries, L. Fong, L. P. Levine, M. Franco, A. Oglesby, C. Ballesteros-Merino, C. B. Bifulco, B. A. Fox, D. Bannavong, R. Talia, E. Browning, M. H. Le, R. H. Pierce, S. Gargosky, K. K. Tsai, C. Twitty, A. I. Daud, Intratumoral delivery of tavokinogene telseplasmid yields systemic immune responses in metastatic melanoma patients, *Annals of Oncology*

(2019), doi:10.1016/j.annonc.2019.12.008.

17. J. Strauss, C. R. Heery, J. W. Kim, C. Jochems, R. N. Donahue, A. S. Montgomery, S. McMahon, E. Lamping, J. L. Marte, R. A. Madan, M. Bilusic, M. R. Silver, E. Bertotti, J. Schlom, J. L. Gulley, First-in-human phase I trial of a tumor-targeted cytokine (NHS-IL12) in subjects with metastatic solid tumors, *Clinical Cancer Research* **25**, 99–109 (2019).

18. B. Sangro, G. Mazzolini, J. Ruiz, M. Herraiz, J. Quiroga, I. Herrero, A. Benito, J. Larrache, J. Pueyo, J. C. Subtil, C. Olagüe, J. Sola, B. Sádaba, C. Lacasa, I. Melero, C. Qian, J. Prieto, Phase I trial of intratumoral injection of an adenovirus encoding interleukin-12 for advanced digestive tumors, *Journal of Clinical Oncology* **22**, 1389–1397 (2004).

19. O. Hamid, M. Hellman, B. Carneiro, T. Marron, V. Subbiah, I. Mehmi, J. Eyles, V. Dubois, B. Ridgway, O. Hamid, A. Gasco Hernandez, 19O Preliminary safety, antitumor activity and pharmacodynamics results of HIT-IT MEDI1191 (mRNA IL-12) in patients with advanced solid tumours and superficial lesions, *Annals of Oncology* **32**, S9 (2021).

20. S. N. Smith, R. Schubert, B. Simic, D. Brücher, M. Schmid, N. Kirk, P. C. Freitag, V. Gradinaru, A. Plückthun, The SHREAD gene therapy platform for paracrine delivery improves tumor localization and 3 intratumoral effects of a clinical antibody, *Proc. Natl Acad. Sci. USA* (2021).

21. D. Brücher, N. Kirchhammer, S. N. Smith, J. Schumacher, N. Schumacher, J. Kolibius, P. C. Freitag, M. Schmid, F. Weiss, C. Keller, M. Grove, U. F. Greber, A. Zippelius, A. Plückthun, iMATCH: an integrated modular assembly system for therapeutic combination high-capacity adenovirus gene therapy, *Molecular Therapy - Methods & Clinical Development* **20**, 572–586 (2021).

22. M. Schmid, P. Ernst, A. Honegger, M. Suomalainen, M. Zimmermann, L. Braun, S. Stauffer, C. Thom, B. Dreier, M. Eibauer, A. Kipar, V. Vogel, U. F. Greber, O. Medalia, A. Plückthun, Adenoviral vector with shield and adapter increases tumor specificity and escapes liver and immune control, *Nature Communications* **9**, 1–16 (2018).

23. Y. Goltsev, N. Samusik, J. Kennedy-Darling, S. Bhate, M. Hale, G. Vazquez, S. Black, G. P. Nolan, Deep Profiling of Mouse Splenic Architecture with CODEX Multiplexed Imaging, *Cell* **174**, 968-981.e15 (2018).

24. M. A. Morris, D. R. Gibb, F. Picard, V. Brinkmann, M. Straume, K. Ley, Transient T cell accumulation in lymph nodes and sustained lymphopenia in mice treated with FTY720, *European Journal of Immunology* **35**, 3570–3580 (2005).

25. L. F. De Andrade, Y. Lu, A. Luoma, Y. Ito, D. Pan, J. W. Pyrdol, C. H. Yoon, G. C. Yuan, K. W. Wucherpfennig, Discovery of specialized NK cell populations infiltrating human melanoma metastases, *JCI Insight* **4** (2019), doi:10.1172/jci.insight.133103.

26. D. Brownlie, M. Scharenberg, J. E. Mold, J. Hard, E. Kekalainen, M. Buggert, S. Nguyen, J. N. Wilson, M. Al-Ameri, H. G. Ljunggren, N. Marquardt, J. Michaelsson, Expansions of adaptive-like NK cells with a tissue-resident phenotype in human lung and blood, *Proceedings of the National Academy of Sciences of the United States of America* **118** (2021), doi:10.1073/pnas.2016580118.

27. A. Crinier, P. Milpied, B. Escalière, C. Piperoglou, J. Galluso, A. Balsamo, L. Spinelli, I. Cervera-Marzal, M. Ebbo, M. Girard-Madoux, S. Jaeger, E. Bollon, S. Hamed, J. Hardwigsen, S. Ugolini, F. Vély, E. Narni-Mancinelli, E. Vivier, High-Dimensional Single-Cell Analysis Identifies Organ-Specific Signatures and Conserved NK Cell Subsets in Humans and Mice, *Immunity* **49**, 971-986.e5 (2018).

28. L. Chiossone, J. Chaix, N. Fuseri, C. Roth, E. Vivier, T. Walzer, Maturation of mouse NK cells is a 4-stage developmental program, *Blood* **113**, 5488–5496 (2009).

29. E. Hashemi, S. Malarkannan, Tissue-Resident NK Cells: Development, Maturation, and Clinical Relevance, *Cancers* **12**, 1–23 (2020).

30. K. Hildner, B. T. Edelson, W. E. Purtha, M. Diamond, H. Matsushita, M. Kohyama, B. Calderon, B. U. Schraml, E. R. Unanue, M. S. Diamond, R. D. Schreiber, T. L. Murphy, K. M. Murphy, Batf3 deficiency reveals a critical role for CD8α+ dendritic cells in cytotoxic T cell immunity, *Science* **322**, 1097–1100 (2008).

31. M. Natoli, N. Bonito, J. D. Robinson, S. Ghaem-Maghami, Y. Mao, Human ovarian cancer intrinsic

mechanisms regulate lymphocyte activation in response to immune checkpoint blockade, *Cancer Immunology, Immunotherapy* **69**, 1391–1401 (2020).

32. P. Voabil, M. de Bruijn, L. Roelofsen, S. Hendriks, S. Brokamp, M. van den Braber, A. Broeks, J. Sanders, P. Herzig, A. Zippelius, C. Blank, K. Hartemink, K. Monkhorst, J. Haanen, T. Schumacher, D. Thommen, An ex vivo tumor fragment platform to dissect response to PD-1 blockade in cancer, *Nature medicine* **27**, 1250–1261 (2021).

33. R. Zilionis, C. Engblom, C. Pfirschke, V. Savova, D. Zemmour, H. D. Saatcioglu, I. Krishnan, G. Maroni, C. V. Meyerovitz, C. M. Kerwin, S. Choi, W. G. Richards, A. De Rienzo, D. G. Tenen, R. Bueno, E. Levantini, M. J. Pittet, A. M. Klein, Single-Cell Transcriptomics of Human and Mouse Lung Cancers Reveals Conserved Myeloid Populations across Individuals and Species, *Immunity* **50**, 1317-1334.e10 (2019).

34. J. Hanna, P. Bechtel, Y. Zhai, F. Youssef, K. McLachlan, O. Mandelboim, Novel Insights on Human NK Cells' Immunological Modalities Revealed by Gene Expression Profiling, *The Journal of Immunology* **173**, 6547–6563 (2004).

35. N. Marquardt, E. Kekäläinen, P. Chen, M. Lourda, J. N. Wilson, M. Scharenberg, P. Bergman, M. Al-Ameri, J. Hård, J. E. Mold, H. G. Ljunggren, J. Michaëlsson, Unique transcriptional and protein-expression signature in human lung tissue-resident NK cells, *Nature Communications* **10**, 1–12 (2019).

36. N. Riaz, J. J. Havel, V. Makarov, A. Desrichard, W. J. Urba, J. S. Sims, F. S. Hodi, S. Martín-Algarra, R. Mandal, W. H. Sharfman, S. Bhatia, W. J. Hwu, T. F. Gajewski, C. L. Slingluff, D. Chowell, S. M. Kendall, H. Chang, R. Shah, F. Kuo, L. G. T. Morris, J. W. Sidhom, J. P. Schneck, C. E. Horak, N. Weinhold, T. A. Chan, Tumor and Microenvironment Evolution during Immunotherapy with Nivolumab, *Cell* **171**, 934-949.e15 (2017).

37. P. Voabil, M. de Bruign, L. M. Roelofsen, S. H. Hendriks, S. Brokamp, M. van den Braber, A. Broeks, J. Sanders, P. Herzig, A. Zippelius, C. U. Blank, K. J. Hartemink, K. Monkhorst, J. Haanen, T. N. Schumacher, D. S. Thommen, Immunological response of human cancers to PD-1 blockade, *Nature Medicine* .

38. M. Sade-Feldman, Defining T cell states associated with response to checkpoint immunotherapy in melanoma, *Cell* **175**, 998–1013 (2018).

39. R. B. Mokhtari, T. S. Homayouni, N. Baluch, E. Morgatskaya, S. Kumar, B. Das, H. Yeger, Combination therapy in combating cancer*Oncotarget* **8**, 38022–38043 (2017).

40. J. Sun, Q. Wei, Y. Zhou, J. Wang, Q. Liu, H. Xu, A systematic analysis of FDA-approved anticancer drugs, *BMC Systems Biology* **11** (2017), doi:10.1186/s12918-017-0464-7.

41. F. Meric-Bernstam, J. Larkin, J. Tabernero, C. Bonini, Enhancing anti-tumour efficacy with immunotherapy combinations, *The Lancet* (2020), doi:10.1016/s0140-6736(20)32598-8.

42. A. P. Algazi, C. G. Twitty, K. K. Tsai, M. Le, R. Pierce, E. Browning, R. Hermiz, D. A. Canton, D. Bannavong, A. Oglesby, M. Francisco, L. Fong, M. J. Pittet, S. P. Arlauckas, C. Garris, L. P. Levine, C. Bifulco, C. Ballesteros-Merino, S. Bhatia, S. Gargosky, R. H. I. Andtbacka, B. A. Fox, M. D. Rosenblum, A. I. Daud, Phase II Trial of IL-12 Plasmid Transfection and PD-1 Blockade in Immunologically Quiescent Melanoma, *Clinical Cancer Research* **26**, 2827–2837 (2020).

43. R. S. Riley, C. H. June, R. Langer, M. J. Mitchell, Delivery technologies for cancer immunotherapy*Nature Reviews Drug Discovery* **18**, 175–196 (2019).

44. B. Dreier, A. Honegger, C. Hess, G. Nagy-Davidescu, P. R. E. Mittl, M. G. Grütter, N. Belousova, G. Mikheeva, V. Krasnykh, A. Plückthun, Development of a generic adenovirus delivery system based on structure-guided design of bispecific trimeric DARPin adapters, *Proceedings of the National Academy of Sciences of the United States of America* **110** (2013), doi:10.1073/pnas.1213653110.

45. B. Dreier, A. Plückthun, Rapid selection of high-affinity binders using ribosome display, *Methods in Molecular Biology* **805**, 261–286 (2012).

46. A. Plückthun, Designed ankyrin repeat proteins (DARPins): Binding proteins for research, diagnostics, and therapy*Annual Review of Pharmacology and Toxicology* **55**, 489–511 (2015).

47. M. Yan, B. A. Parker, R. Schwab, R. Kurzrock, HER2 aberrations in cancer: Implications for therapy*Cancer Treatment Reviews* **40**, 770–780 (2014).

48. S. Kakarla, X. T. Song, S. Gottschalk, Cancer-associated fibroblasts as targets for immunotherapy*Immunotherapy* **4**, 1129–1138 (2012).

49. M. Trüb, F. Uhlenbrock, C. Claus, P. Herzig, M. Thelen, V. Karanikas, M. Bacac, M. Amann, R. Albrecht, C. Ferrara-Koller, D. Thommen, S. Rothschield, S. Savic, K. D. Mertz, G. Cathomas, R. Rosenberg, V. Heinzelmann-Schwarz, M. Wiese, D. Lardinois, P. Umana, C. Klein, H. Laubli, A. S. Kashyap, A. Zippelius, Fibroblast activation protein-targeted-4-1BB ligand agonist amplifies effector functions of intratumoral T cells in human cancer, *J Immunother Cancer* **8**, 238 (2020).

50. D. Muruve, V. Pétrilli, A. Zaiss, L. White, S. C.- Nature, undefined 2008, The inflammasome recognizes cytosolic microbial and host DNA and triggers an innate immune response, *nature.com* (available at https://idp.nature.com/authorize/casa?redirect_uri=https://www.nature.com/articles/nature06664&casa_token=qEgbTzaHI1wAAAAA:tFfSt0FGmMP38ukR8KLDmvdRRln9cyoNzrRMTJOJGxa6nggKlZH7TZYonHfJitttXsgg0B5V5U-0KdEtfw).

51. D. M. Appledorn, S. Patial, S. Godbehere, N. Parameswaran, A. Amalfitano, TRIF, and TRIF-interacting TLRs differentially modulate several adenovirus vector-induced immune responses, *Journal of Innate Immunity* **1**, 376–388 (2009).

52. and Andrea Amalfitano Godbehere, N. Van Rooijen, N. M. Parameswaran Daniel Appledorn, S. Patial, A. McBride, Vivo Dependent upon Both TLR2 and TLR9 In As Well As Adaptive Immune Responses Are Inflammatory Mediators, MAPK Signaling, Adenovirus Vector-Induced Innate, *Am Assoc Immnol* (2021), doi:10.4049/jimmunol.181.3.2134.

53. Z. Urban-Wojciuk, M. M. Khan, B. L. Oyler, R. Fåhraeus, N. Marek-Trzonkowska, A. Nita-Lazar, T. R. Hupp, D. R. Goodlett, The role of tlrs in anti-cancer immunity and tumor rejection, *Frontiers in Immunology* **10**, 2388 (2019).

54. M. Budhwani, R. Mazzieri, R. Dolcetti, Plasticity of type I interferon-mediated responses in cancer therapy: From anti-tumor immunity to resistance*Frontiers in Oncology* **8**, 322 (2018).

55. R. Saleh, E. Elkord, Acquired resistance to cancer immunotherapy: Role of tumor-mediated immunosuppression, *Seminars in cancer biology* **65**, 13–27 (2020).

56. S. Spranger, D. Dai, B. Horton, T. F. Gajewski, Tumor-Residing Batf3 Dendritic Cells Are Required for Effector T Cell Trafficking and Adoptive T Cell Therapy, *Cancer Cell* **31**, 711-723.e4 (2017).

57. C. Degos, M. Heinemann, J. Barrou, N. Boucherit, E. Lambaudie, A. Savina, L. Gorvel, D. Olive, Endometrial Tumor Microenvironment Alters Human NK Cell Recruitment, and Resident NK Cell Phenotype and Function, *Frontiers in Immunology* **0**, 877 (2019).

58. L. Ducimetière, G. Lucchiari, G. Litscher, M. Nater, L. Heeb, N. G. Nuñez, L. Wyss, D. Burri, M. Vermeer, J. Gschwend, A. E. Moor, B. Becher, M. van den Broek, S. Tugues, Conventional NK cells and tissue-resident ILC1s join forces to control liver metastasis, *Proceedings of the National Academy of Sciences* **118**, e2026271118 (2021).

59. H. Sun, L. Liu, Q. Huang, H. Liu, M. Huang, J. Wang, H. Wen, R. Lin, K. Qu, K. Li, H. Wei, W. Xiao, R. Sun, Z. Tian, C. Sun, Accumulation of Tumor-Infiltrating CD49a + NK Cells Correlates with Poor Prognosis for Human Hepatocellular Carcinoma, *Cancer immunology research* **7**, 1535–1546 (2019).

60. T. T. Murooka, R. Rahbar, E. N. Fish, CCL5 promotes proliferation of MCF-7 cells through mTOR-dependent mRNA translation, *Biochemical and Biophysical Research Communications* **387**, 381–386 (2009).

61. N. Casagrande, C. Borghese, L. Visser, M. Mongiat, A. Colombatti, D. Aldinucci, CCR5 antagonism by maraviroc inhibits hodgkin lymphoma microenvironment interactions and xenograft growth, *Haematologica* **104**, 564–575 (2019).

62. A. E. Karnoub, A. B. Dash, A. P. Vo, A. Sullivan, M. W. Brooks, G. W. Bell, A. L. Richardson, K. Polyak, R. Tubo, R. A. Weinberg, Mesenchymal stem cells within tumour stroma promote breast cancer metastasis, *Nature* **449**, 557–563 (2007).

63. X. Jiao, M. A. Velasco-Velazquez, M. Wang, Z. Li, H. Rui, A. R. Peck, J. E. Korkola, X. Chen, S. Xu, J. B. DuHadaway, S. Guerrero-Rodriguez, S. Addya, D. Sicoli, Z. Mu, G. Zhang, A. Stucky, X. Zhang, M. Cristofanilli, A. Fatatis, J. W. Gray, J. F. Zhong, G. C. Prendergast, R. G. Pestell, CCR5 Governs DNA damage repair and breast cancer stem cell expansion, *Cancer Research* **78**, 1657–1671 (2018).

64. P. Debré, B. Combadiere, A. Boissonnas, O. Bonduelle, M. Maho, E. Lavergne, C. Combadière, M. Iga, Increases Tumor Cell Infiltration Overexpression Delays Tumor Growth and Intratumoral CC Chemokine Ligand 5, *J Immunol References* **173**, 3755–3762 (2021).

65. D. Dangaj, M. Bruand, A. J. Grimm, C. Ronet, D. Barras, P. A. Duttagupta, E. Lanitis, J. Duraiswamy, J. L. Tanyi, F. Benencia, J. Conejo-Garcia, H. R. Ramay, K. T. Montone, D. J. Powell, P. A. Gimotty, A. Facciabene, D. G. Jackson, J. S. Weber, S. J. Rodig, S. F. Hodi, L. E. Kandalaft, M. Irving, L. Zhang, P. Foukas, S. Rusakiewicz, M. Delorenzi, G. Coukos, Cooperation between Constitutive and Inducible Chemokines Enables T Cell Engraftment and Immune Attack in Solid Tumors, *Cancer Cell* **35**, 885-900.e10 (2019).

66. J. M. Romero, B. T. Grünwald, G.-H. Jang, P. P. Bavi, A. Jhaveri, M. Masoomian, S. E. Fischer, A. Zhang, R. E. Denroche, I. M. Lungu, A. De Luca, J. M. S. Bartlett, J. Xu, N. Li, S. Dhaliwal, S.-B. Liang, D. Chadwick, F. Vyas, P. Bronsert, R. Khokha, T. L. McGaha, F. Notta, P. S. Ohashi, S. J. Done, G. M. O'Kane, J. M. Wilson, J. J. Knox, A. Connor, Y. Wang, G. Zogopoulos, S. Gallinger, A four-chemokine signature is associated with a T cell-inflamed phenotype in primary and metastatic pancreatic cancer, *Clinical Cancer Research* , clincanres.2803.2019 (2020).

67. N. Jacquelot, C. Seillet, E. Vivier, G. T. Belz, Innate lymphoid cells and cancer, *Nature Immunology 2022 23:3* **23**, 371–379 (2022).

68. V. S. Cortez, T. K. Ulland, L. Cervantes-Barragan, J. K. Bando, M. L. Robinette, Q. Wang, A. J. White, S. Gilfillan, M. Cella, M. Colonna, SMAD4 impedes the conversion of NK cells into ILC1-like cells by curtailing non-canonical TGF-β signaling, *Nature immunology* **18**, 995–1003 (2017).

69. L. F. de Andrade, Y. Lu, A. Luoma, Y. Ito, D. Pan, J. W. Pyrdol, C. H. Yoon, G.-C. Yuan, K. W. Wucherpfennig, Discovery of specialized NK cell populations infiltrating human melanoma metastases, *JCI Insight* **4** (2019), doi:10.1172/JCI.INSIGHT.133103.

70. J. Luo, Z. L. Deng, X. Luo, N. Tang, W. X. Song, J. Chen, K. A. Sharff, H. H. Luu, R. C. Haydon, K. W. Kinzler, B. Vogelstein, T. C. He, A protocol for rapid generation of recombinant adenoviruses using the AdEasy system, *Nature Protocols* **2**, 1236–1247 (2007).

71. L. D'Amico, U. Menzel, M. Prummer, P. Müller, M. Buchi, A. Kashyap, U. Haessler, A. Yermanos, R. Gébleux, M. Briendl, T. Hell, F. I. Wolter, R. R. Beerli, I. Truxova, Š. Radek, T. Vlajnic, U. Grawunder, S. Reddy, A. Zippelius, A novel anti-HER2 anthracycline-based antibody-drug conjugate induces adaptive anti-tumor immunity and potentiates PD-1 blockade in breast cancer, *Journal for ImmunoTherapy of Cancer* **7**, 16 (2019).

72. flowCore: flowCore: Basic structures for flow cytometry data version 2.2.0 from Bioconductor (available at https://rdrr.io/bioc/flowCore/).

73. CATALYST: Cytometry dATa anALYSis Tools version 1.14.0 from Bioconductor (available at https://rdrr.io/bioc/CATALYST/).

74. GitHub - JinmiaoChenLab/Rphenograph: Rphenograph: R implementation of the PhenoGraph algorithm (available at https://github.com/JinmiaoChenLab/Rphenograph).

75. J. H. Levine, E. F. Simonds, S. C. Bendall, K. L. Davis, E. A. D. Amir, M. D. Tadmor, O. Litvin, H. G. Fienberg, A. Jager, E. R. Zunder, R. Finck, A. L. Gedman, I. Radtke, J. R. Downing, D. Pe'er, G. P. Nolan, Data-Driven Phenotypic Dissection of AML Reveals Progenitor-like Cells that Correlate with Prognosis, *Cell* **162**, 184–197 (2015).

76. CRAN - Package pheatmap (available at https://cran.r-project.org/web/packages/pheatmap/index.html).

77. GitHub - BIOP/ijp-kheops (available at https://github.com/BIOP/ijp-kheops).

78. GitHub - stardist/stardist: StarDist - Object Detection with Star-convex Shapes (available at https://github.com/stardist/stardist).

79. P. Bankhead, M. B. Loughrey, J. A. Fernández, Y. Dombrowski, D. G. McArt, P. D. Dunne, S. McQuaid, R. T. Gray, L. J. Murray, H. G. Coleman, J. A. James, M. Salto-Tellez, P. W. Hamilton, QuPath: Open source software for digital pathology image analysis, *Scientific Reports* **7** (2017), doi:10.1038/s41598-017-17204-5.

80. N. Samusik, Z. Good, M. H. Spitzer, K. L. Davis, G. P. Nolan, Automated mapping of phenotype space with single-cell data, *Nature Methods* **13**, 493–496 (2016).

81. I. Tirosh, B. Izar, S. M. Prakadan, M. H. Wadsworth, D. Treacy, J. J. Trombetta, A. Rotem, C. Rodman, C. Lian, G. Murphy, M. Fallahi-Sichani, K. Dutton-Regester, J. R. Lin, O. Cohen, P. Shah, D. Lu, A. S. Genshaft, T. K. Hughes, C. G. K. Ziegler, S. W. Kazer, A. Gaillard, K. E. Kolb, A. C. Villani, C. M. Johannessen, A. Y. Andreev, E. M. Van Allen, M. Bertagnolli, P. K. Sorger, R. J. Sullivan, K. T. Flaherty, D. T. Frederick, J. Jané-Valbuena, C. H. Yoon, O. Rozenblatt-Rosen, A. K. Shalek, A. Regev, L. A. Garraway, Dissecting the multicellular ecosystem of metastatic melanoma by single-cell RNA-seq, *Science* **352**, 189–196 (2016).

82. F. Souza-Fonseca-Guimaraes, J. Cursons, N. D. Huntington, The Emergence of Natural Killer Cells as a Major Target in Cancer Immunotherapy*Trends in Immunology* (2019), doi:10.1016/j.it.2018.12.003.

Acknowledgments

We thank members of the Cancer Immunology and Cancer Immunotherapy Laboratory at the Department of Biomedicine for helpful discussions and suggestions. We are grateful to A. Ignatenco and B. Simic for cloning viral constructs and to F. Weiss, and P. Freitag for producing and providing the biological reagents. We thank Priska Auf der Maur (University Hospital of Basel) for designing the graphical abstract. This work benefited from clinical data provided by OncoSec Medical Incoporated.

Funding

This work was funded by the Schweizerische Nationalfonds Grant CRSII5_170929 to A.Z. and A.P., by the Schweizerische Nationalfonds Grant 320030_188576/1 to A.Z., by the National Cancer Institute of the National Institutes of Health under award number F32CA189372 (to S.N.S.), by the University of Zurich Forschungskredit 2017 ID 3761 (to D.B.), and by the Cancer League beider Basel Grant KLbB-5325-03-2021 (to N.K.).

Authors contributions

N.K. designed the study, performed experiments, analyzed data, and wrote the manuscript. M.P.T. (in vitro), M.N. (in vitro), F.W., V.K., M.B. (in vivo), and D.S.T. (in vitro) planned and performed experiments and generated and analyzed data. D.B., S.N.S., D.B., K.P.H, and P.Z. designed, cloned, or produced biological reagents. D.S. and E.B. processed and analyzed data. M.P.T., M.N., D.B., S.N.S., H.L., J.P.B., M.A.S., A.S.K., and A.P. provided input for research design and interpretation and edited the manuscript. A.Z. directed the study and wrote the manuscript. All authors reviewed and approved the manuscript.

Competing interests

A.P. is a cofounder, consultant and shareholder and N.K., D.B. and S.N.S. are employees and shareholders of Vector BioPharma, which is commercializing the Shielded Retargeted Adenovirus (SHREAD) technology. V.K. is employee of SIRION Biotech GmbH. A.Z. received consulting/advisor fees from BMS, MSD, Hoffmann–La Roche, NBE Therapeutics, Secarna, ACM Pharma, and Hookipa, and maintains further non-commercial research agreements with Secarna, Hookipa, and Beyondsprings. No potential conflicts of interest were disclosed by the other authors.

Data and material availability

All data associated with this study are in the paper or supplementary materials. The previously published RNAseq and scRNAseq data sets we re-analyzed are accessible at GEO under accession number GSE91061, GSE120575 and GSE127465, respectively. Source data and all other supporting data of this study are available from the corresponding authors on a reasonable request. Codes used for the analysis of flow cytometry data and multidimensional IF microscopy in Fig. 1, as well as the analysis of published expression data can be obtained from the corresponding authors upon request. Viral vectors, adapters and shield are available from Andreas Plückthun under a material transfer agreement with the University of Zurich.

Figures

Fig. 1: IL-12 immunotherapy prompts NK cells to orchestrate an anti-tumor microenvironment

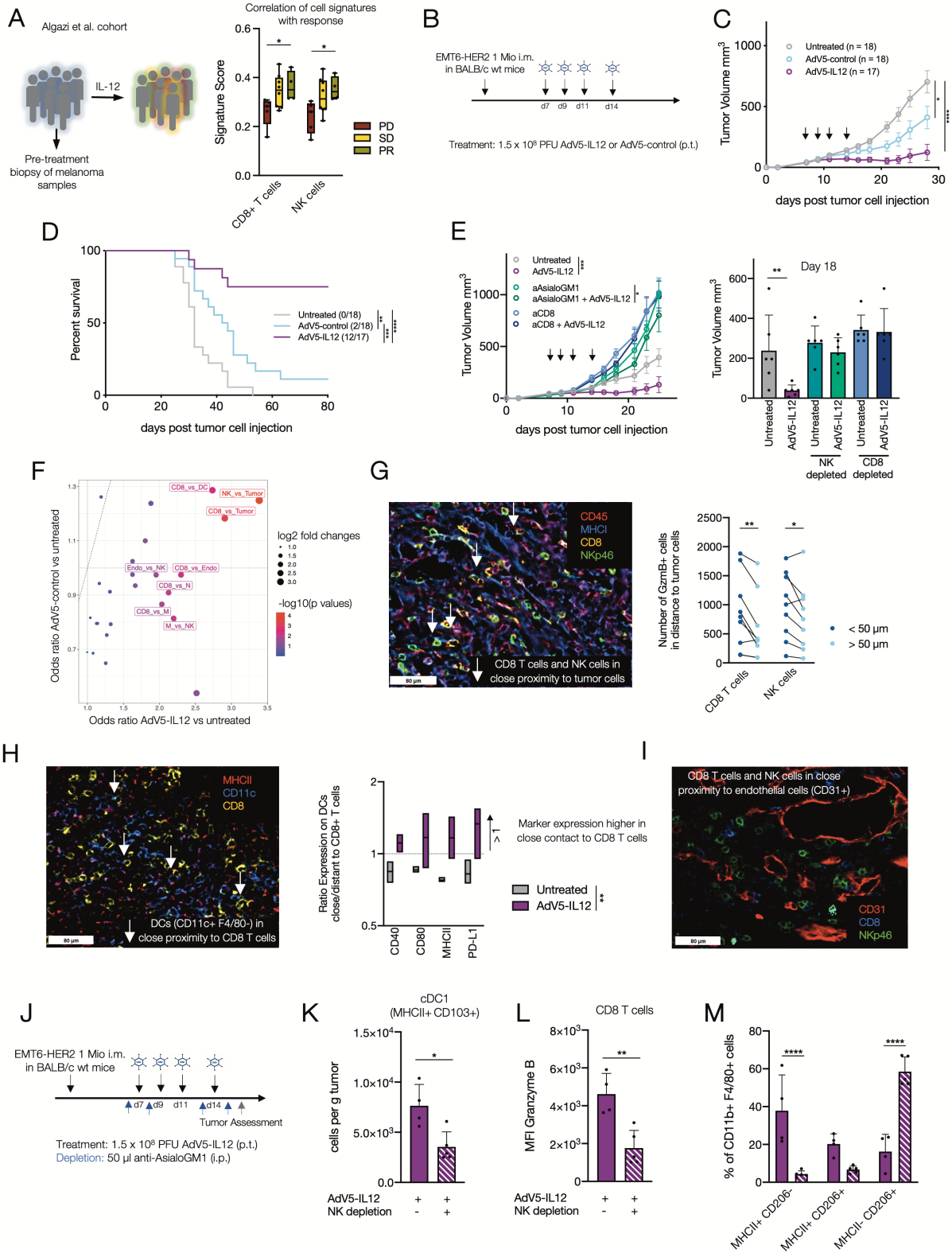

(**A**) Cell signature scores measured by Nanostring in skin tumor biopsies from 19 patients with melanoma before intra-tumoral treatment with ImmunoPulse IL-12 were correlated with clinical response (PD: progressive disease, SD: stable disease, PR: partial response) *(16)*. (**B**)Wildtype (WT) mice were engrafted

with $1x10^6$ EMT6-HER2 intramammarily (i.m.). From day 7 (tumor size 30–70 mm^3), mice were treated with $1.5x10^8$ PFU of HER2-targeted and shielded adenoviral vectors (peritumorally, p.t.) encoding for IL-12 or an empty control cassette (AdV5-control) on days 7, 9, 11 and 14 p.t. indicated by black arrows (**C**)Tumor growth and (**D**) Kaplan-Meier survival curves are shown with the number of mice indicated. Black arrows denote days of treatment. Pooled data from at least three independent experiments. (E) For depletion studies, mice were injected i.p. with anti-CD8 and anti-AsialoGM1 starting one day before adenoviral treatment. Tumor growth curves after depletion are shown. Black arrows denote days of adenoviral treatment. Pooled data from two independent experiments. *n* = 6-12 mice. (**F**) Visualization of odds ratios and -log10(p values) for changes in cell-cell type interactions between experimental conditions focusing on interaction including CD8 T cells and NK cells. *n* = 3 mice per condtion. Each one section was acquired. *N* = 1. (**G**) Representative IF pictures are showing AdV5-IL12 treated tumors (CD45: red, MHCI: blue, CD8: yellow, NKp46: green). White arrows are showing CD8 T cells (CD45+, MHCI+, CD8+) or NK cells (CD45+, MHCI+, NKp46+) neighboring tumor cells (CD45-, MHCI+). Quantification of GzmB+ CD8 T cells and NK cells in close proximity (<50 µm) to tumor cells in comparison to more distant (>50 µm) proximity. Each dot represents the count in one acquired tumor. Treatment conditions were pooled in this analysis. *N* = 1. (**H**) Representative IF pictures are showing AdV5-IL12 treated tumors (MHCII: red, CD11c: blue, CD8: yellow). White arrows are showing CD8 T cells (CD45+, CD8+) neighboring DCs (CD45+, CD11c+, F4/80-). Ratio of CD40, CD80, MHCII and PD-L1 expression on the DC cluster in close (<50 µm) or distant (>50 µm) proximity to CD8 T cell cluster comparing untreated and AdV5-IL12 treated tumors are shown. (**I**) Representative IF pictures showing CD8 T cells and NK cells in close proximity to blood vessels in AdV5-IL12 treated tumors (CD31: red, CD8: blue, NKp46: green). n = 3 mice per group. (**J**) EMT6-HER2-bearing mice were treated with AdV5-IL-12. NK cells were depleted using anti-AsialoGM1 antibody (i.p) as indicated (blue arrow). Tumors were isolated and single cell suspensions of tumors digest were analyzed using flow cytometry on day 16. *N* = 1. (**K**) Intra-tumoral cDC1s (CD11c+, F4/80-, Ly-6G-, MHCII+, CD103+, $CD11b^{low}$) were quantified after AdV5-IL12 treatment +/- NK depletion. (**L**) Mean fluorescence intensity (MFI) of granzyme B on CD8 T cells (CD3+, CD8+, NKp46-, CD19-, Ly-6G-). (**M**) Polarization of macrophages (CD11b+ F4/80+) after AdV5-IL12 treatment comparing NK depletion versus non-depleted. k-m: n = 4-5 mice per group. *$P < 0.05$, ** $P < 0.01$, *** $P < 0.001$, **** $P < 0.0001$. Error bar values represent SD or SEM (tumor growth curves). For comparisons between three or more groups, one-way ANOVA with multiple comparisons was used. For survival analysis, *P* values were computed using the Log Rank test. Two-way ANOVA was used to compare tumor growth curves.

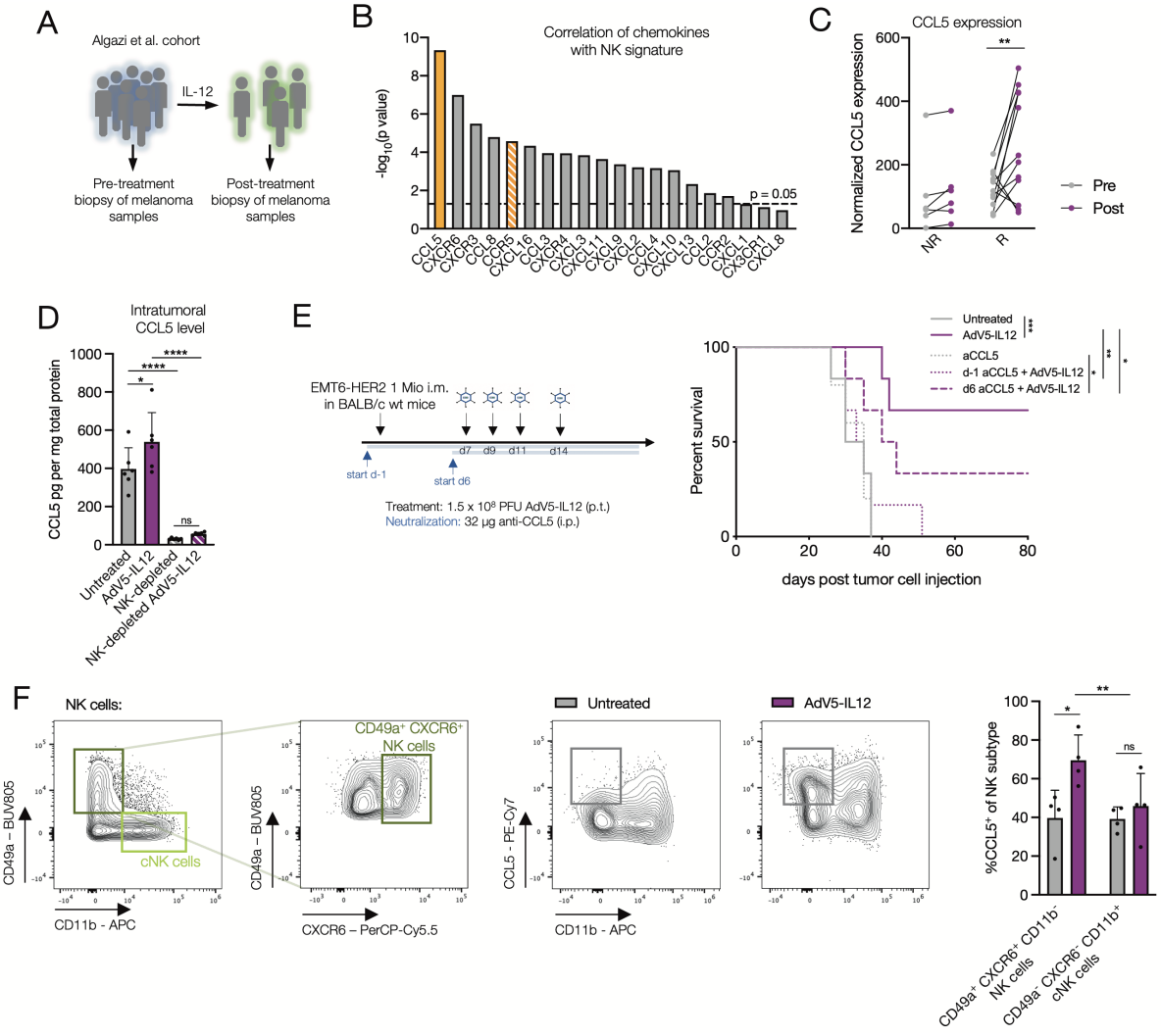

Fig. 2: CCL5, mainly produced by CD49a⁺ CXCR6⁺ NK cells, is required for IL-12 mediated tumor rejection

(**A**) NK cell signature scores measured by Nanostring in skin tumor biopsies from responding patients with melanoma before intra-tumoral treatment with ImmunoPulse IL-12 were correlated with chemokines and their receptor. (**B**) -log10(p value) of chemokines and their receptors which are correlating with NK signature are shown. Values over dotted line are significant. (**C**) Normalized counts of *CCL5* expression of patients with no-response (NR: PD) versus response (R: SD + PR) before and after intra-tumoral treatment with ImmunoPulse IL-12 determined by NanoString. (**D**) EMT6-HER2-engrafted mice (i.m.) were treated with AdV5-IL12 and/or anti-Asialo-GM1 antibody on day 7, 9 and 11 post tumor inoculation, tumors were isolated and lysed. CCL5 expression was determined by ELISA and normalized to total protein measured by bicinchoninic acid assay (BCA). *n*= 6 per condition. 2-tailed Student's t test was used. *N* = 1. (**E**) EMT6-HER2-engrafted mice were treated with AdV5-IL12 following the indicated schedule as shown by the black arrows. Starting one day prior tumor inoculation or one day prior adenoviral therapy, CCL5 was neutralized using antibodies every 3-4 days as shown by the blue arrows. Kaplan-Meier survival curves are shown. *n* = 6. *N* = 1. (**F**) Mice were treated with AdV5-IL12 on day 7, 9 and 11 post EMT6-HER2 inoculation. On day 12 tumors were isolated and CCL5 was analyzed on NK cell subsets (CD49a+ CXCR6+ CD11b- cells or CD49a-CXCR6-CD11b+ cNK cells). *N* = 1. * $P < 0.05$, ** $P < 0.01$, *** $P < 0.001$, **** $P < 0.0001$. Error

bar values represent SD or SEM (tumor growth curves). For comparisons between three or more groups, one-way ANOVA with multiple comparisons was used. For survival analysis, *P* values were computed using the Log Rank test. Two-way ANOVA was used to compare tumor growth curves.

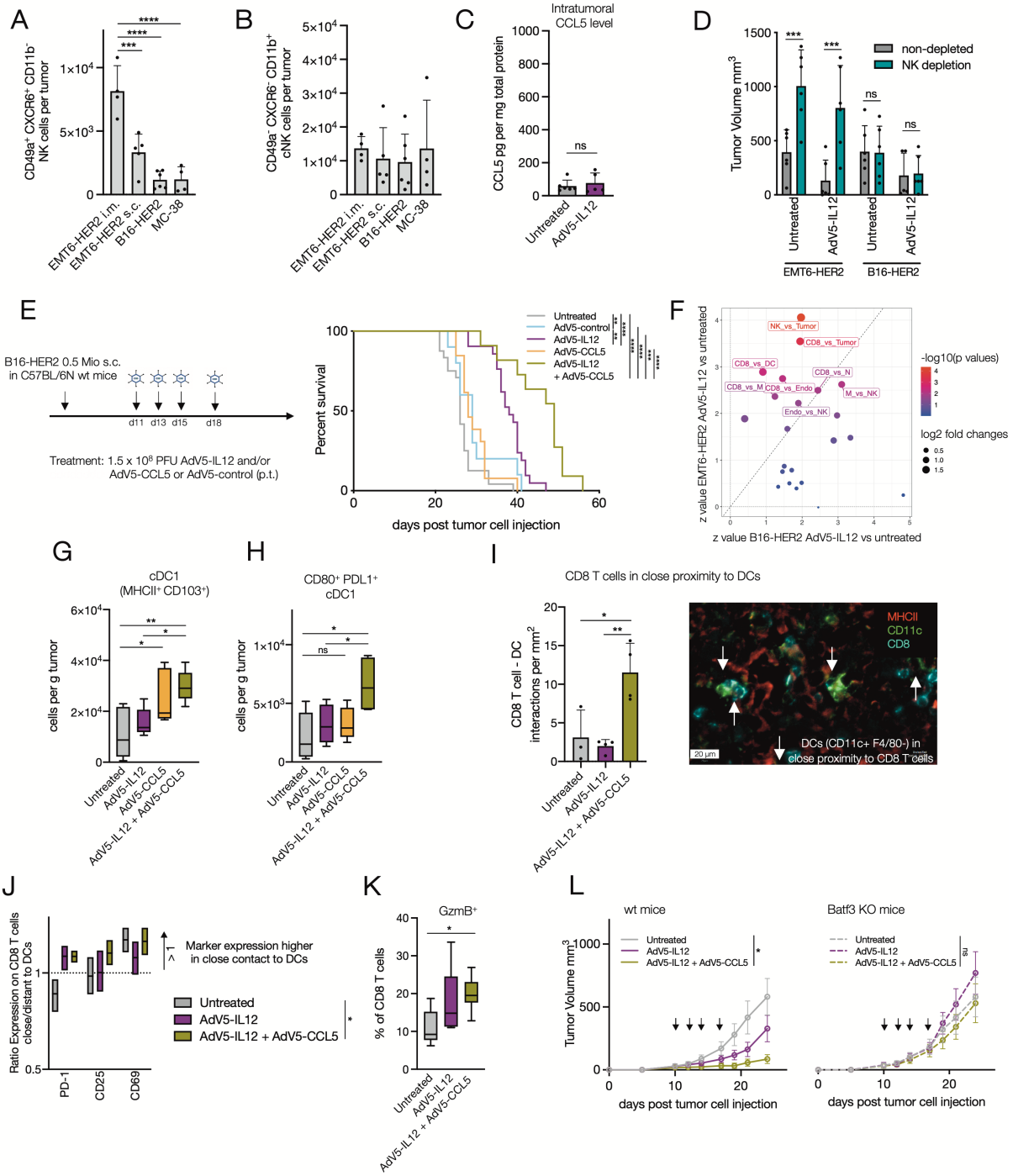

Fig. 3: AdV5-CCL5 overcomes AdV5-IL12 resistance in in CD49a⁺ CXCR6⁺ NK cell poor tumors

(A) Amount of intratumoral CD49a⁺ CXCR6⁺ NK cells tumor was determined in untreated EMT6-HER2 i.m., EMT6-HER2 s.c., B16-HER2 s.c. and MC-38 s.c tumors. *N* = 1. **(B)** Amount of intratumoral cNK cells tumor was determined in untreated EMT6-HER2 i.m., EMT6-HER2 s.c., B16-HER2 s.c. and MC-38 s.c tumors. *N* = 1. **(C)** B16-HER2-engrafted mice were treated with AdV5-IL12 on day 11, 13 and 15 post tumor inoculation, tumors were isolated and lysed on day 16. CCL5 expression was determined by ELISA and normalized to total protein measured by BCA. *n*= 6 per condition. *N* = 1. **(D)** Wildtype (WT) mice were engrafted with 1 mio EMT6-HER2 (i.m.) or 0.5 mio B16-HER2 (s.c.). Mice were treated with AdV5-IL12 on

day 7, 9, 11 and 14 or day 11, 13, 15 and 18 (tumor size 30–70 mm^3), respectively. NK cells were depleted using anti-AsialoGM1 and anti-NK1.1 antibody every 4-5 days starting one day prior adenoviral therapy. Tumor volume on day 25 post tumor inoculation is shown. *N* = 1. (**E**) Mice were treated with AdV5-IL12 and AdV5-CCL5 on day 11, 13, 15 and 18 (tumor size 30–70 mm^3) after B16-HER2 inoculation as indicated by the black arrow: Kaplan-Meier survival curves are shown. *n* > 15 mice per condition. Pooled data from at least three independent experiments. (**F**) Mice were engrafted with 1 mio EMT6-HER2 (i.m.) or 0.5 mio B16-HER2 (s.c.). Starting from day 7 or 11 (tumor size 30–70 mm^3), mice were treated with $1.5x10^8$ PFU of HER2-targeted and shielded adenoviral vectors (p.t.) encoding for IL-12 on day 7/11, 9/13 and 11/15. On day 12/16 post inoculation, tumors were isolated, embedded in OCT and analyzed by multiparameter immuno-fluorescence microscopy. *N* = 1. Visualization of odds ratios and *P* values for changes in cell-cell type interactions between EMT6-HER2 versus B16-HER2 focusing on interaction including CD8 T cells and NK cells. (**G:** Mice were engrafted with 0.5 mio B16-HER2 (s.c.). Mice were treated with AdV5-IL12 and/or AdV5-CCL5 on day 11, 13 and 15 (tumor size 30–70 mm^3). On day 16 post inoculation, tumors were isolated and single cell suspensions were analyzed by flow cytometry or embedded in OCT and analyzed by multiparameter immuno-fluorescence microscopy. N = 1. Number of cDC1s (CD11c+, F4/80-, Ly-6G-, MHCII+, CD103+, $CD11b^{low}$) and (H) PD-L1 and CD80 expressing cDC1s, respectively. (**I**) Interaction count per mm^2 of CD8 T cells in close proximity to DCs. Representative IF pictures are showing AdV5-IL12 + AdV5-CCL5 treated tumors (MHCII: red, CD11c: green, CD8: blue). White arrows are showing CD8 T cells (CD45+, CD8+) neighboring DCs (CD45+, CD11c+, F4/80-). (**J**) Ratio of PD-1, CD25 and CD69 expression on the CD8 T cell cluster in close (<50 µm) or distant (>50 µm) proximity to DC cluster. (**K**) Proportion of granzyme B+ of CD8 T cells (CD3+, CD4-, NKp46- CD19-). (**L**) Batf3 knockout mice (lacking cDC1s) were engrafted with 0.5 mio B16-HER2 (s.c.). Mice were treated with AdV5-IL12 and/or AdV5-CCL5. Tumor growth curves are shown. *n* = 11 mice per condition. Pooled data from two independent experiments. **P* < 0.05, ** *P* < 0.01, *** *P* < 0.001, **** *P* < 0.0001. Error bar values represent SEM. For survival analysis, *P* values were computed using the Log Rank test. Two-way ANOVA was used to compare tumor growth curves.

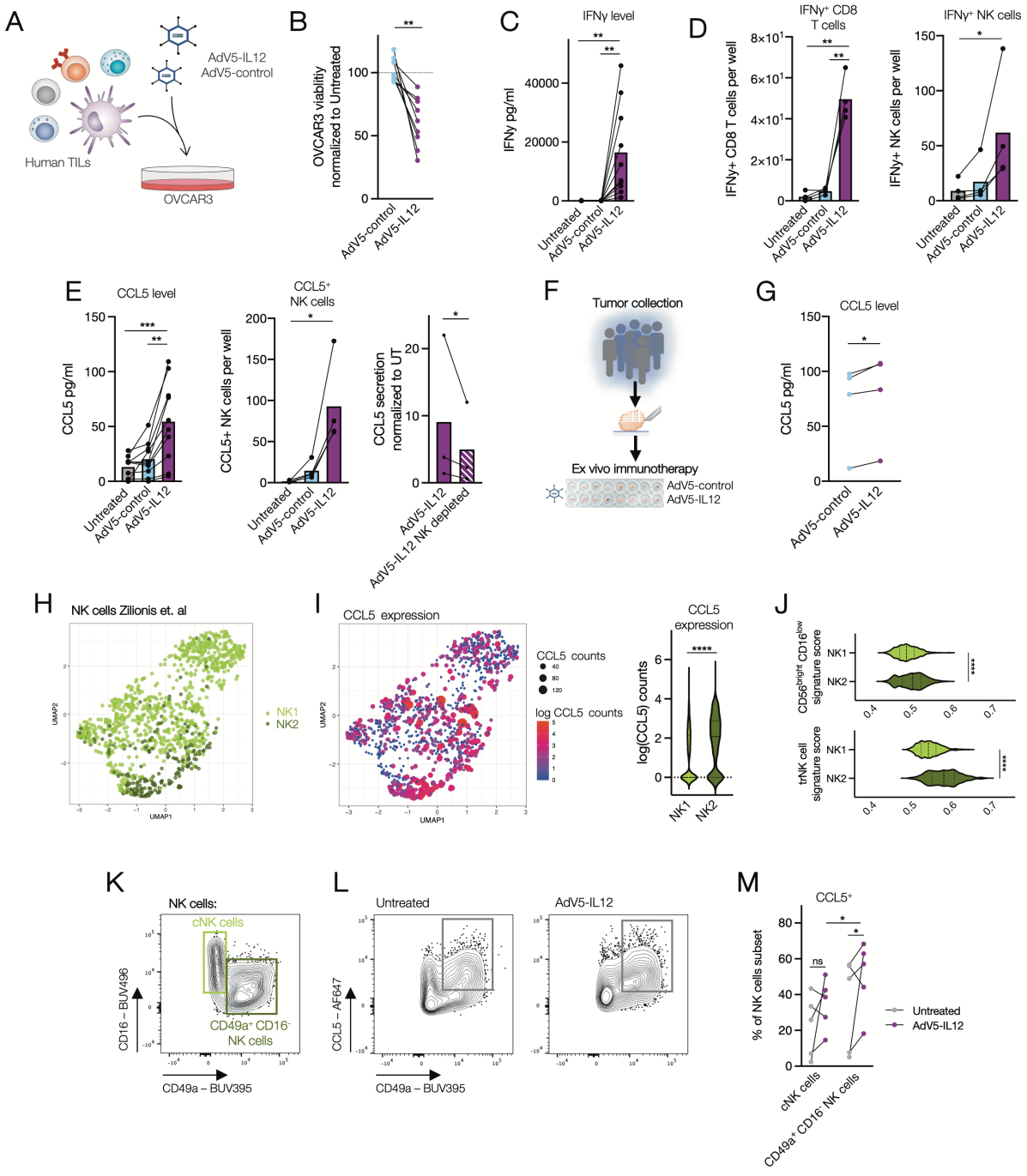

Fig. 4: AdV5-huIL-12 induces CCL5 expression in CD49a$^+$ CD16$^-$ NK cells in patient-derived tumor cultures

(A) Tumor digests of patients with NSCLC were co-cultured with OVCAR-3 cells which were transduced with HER2-targeted AdV5 encoding human IL-12 or control virus. *N* = 2. **(B)** Quantification of OVCAR-3 viability normalized to untreated co-cultures after 96 h. **(C)** IFNγ expression was determined in supernatants after 5d. **(D)** Cell count of IFNγ+ CD8 T cells (CD3+, CD56-) and NK cells (CD56+, CD3-) per well after 96 h. **(E)** Cell count of CCL5+ NK cells (CD56+, CD3-) after 96 h and CCL5 expression in supernatants after 5d. **(F)** HER2+ ovarian cancer samples were dissected into tumor fragments and cultivated embedded in matrigel. Tumor fragments were treated with HER2-targeted AdV5 encoding human IL-12 for 48 h (8-12

fragments per condition). (**G**) CCL5 concentration in supernatant was analyzed by ELISA. (**H**) UMAP projection of scRNASeq data of tumor-infiltrating NK cells of patients with NSCLC is shown. (**I**) *CCL5* expression in NK1 and NK2 subpopulations was quantified. (**J**) $CD56^{bright}CD16^{low}$ and tissue-resident NK (trNK) cell signature scores of NK1 and NK2 were determined. (**K–M**) Tumor digests of patients with NSCLC were co-cultured with OVCAR-3 cells which were transduced with HER2-targeted AdV5 encoding human IL-12. (**K**) NK cell subsets were defined by CD16 and CD49a expression. (**L**) CCL5 producing NK subsets were visualized after AdV5-IL12 treatment (left) compared to untreated (right). (**M**) Percentage of CCL5-positive NK cell subsets were quantified. * $P < 0.05$, ** $P < 0.01$, *** $P < 0.001$, **** $P < 0.0001$. Error bar values represent SD. Paired 2-tailed Student's t test was used. For comparisons between three or more groups, one-way ANOVA with multiple comparisons was used.

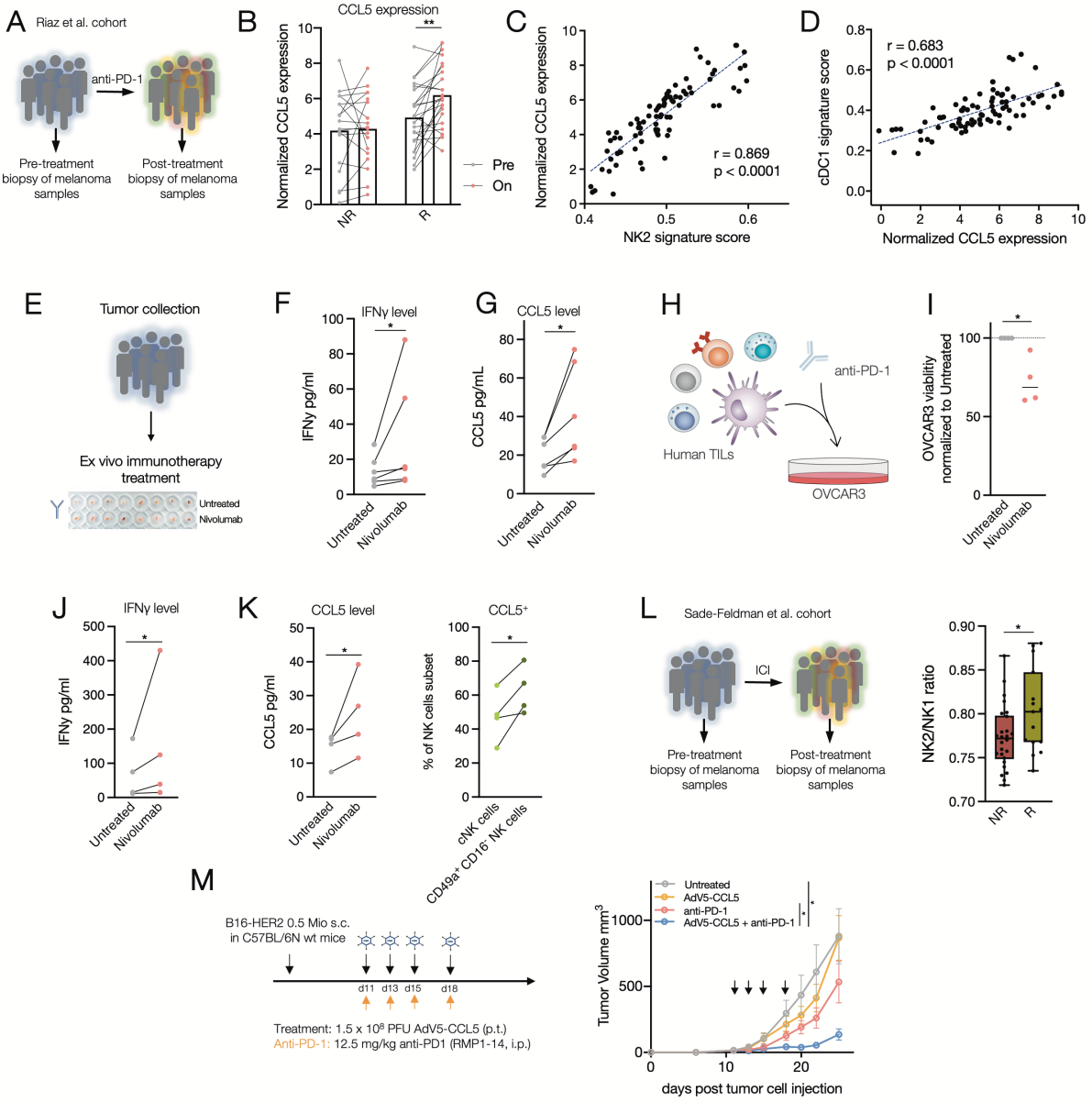

Fig. 5: CCL5 expression by NK cells with tissue-resident traits enhances the efficacy of PD-1 blockade

CCL5 expression in tumor biopsies of patients with melanoma (*n*= 42) was analyzed pre and on nivolumab treatment *(36)*. (**B**) Normalized expression of *CCL5* pre and on nivolumab treatment between patients with no response (NR) or response (R = SD+PR+CR) was quantified. (**C**) Correlation between *CCL5* expression and NK2 signature score or (**D**) cDC1 signature score are shown. (**E**) Cancer samples were dissected into tumor fragments and cultivated embedded in Matrigel. Tumor fragments were treated with nivolumab for 48 h (6-8 fragments per condition). (G) IFNγ and (E) CCL5 were determined in the supernatant. *n* = 6 tumor samples. (**H**) Tumor digests of patients with NSCLC treated with nivolumab were co-cultured with OVCAR-3 cells for 48h. (**I**) OVCAR3 viability was normalized to untreated control group. (**J**) IFNγ and (**K**) CCL5 were determined in the supernatant. Percentage of CCL5 positive NK cells was quantified after nivolumab treatment. (**L**) NK2/NK1 ratio of patients with no-response (NR: PD) versus response (R: SD + PR) before and after treatment with ICI. (**M**) WT mice were engrafted with 0.5 mio B16-HER2 (s.c.). Mice were treated

with AdV5-CCL5 (p.t.) as indicated by black arrows and/or anti-PD-1 (i.p.) antibodies on day 11, 13, 15 and 18 (tumor size 30–70 mm^3) as indicated by orange arrows. Tumor growth curves are shown. n= 6 mice per condition. N = 1. *$P < 0.05$, ** $P < 0.01$, *** $P < 0.001$, **** $P < 0.0001$. Error bar values represent SD or SEM (tumor growth curves). Paired 2-tailed Student's t test was used. For comparisons between three or more groups, one-way ANOVA with multiple comparisons was used. Two-way ANOVA was used to compare tumor growth curves.

Supplementary Materials

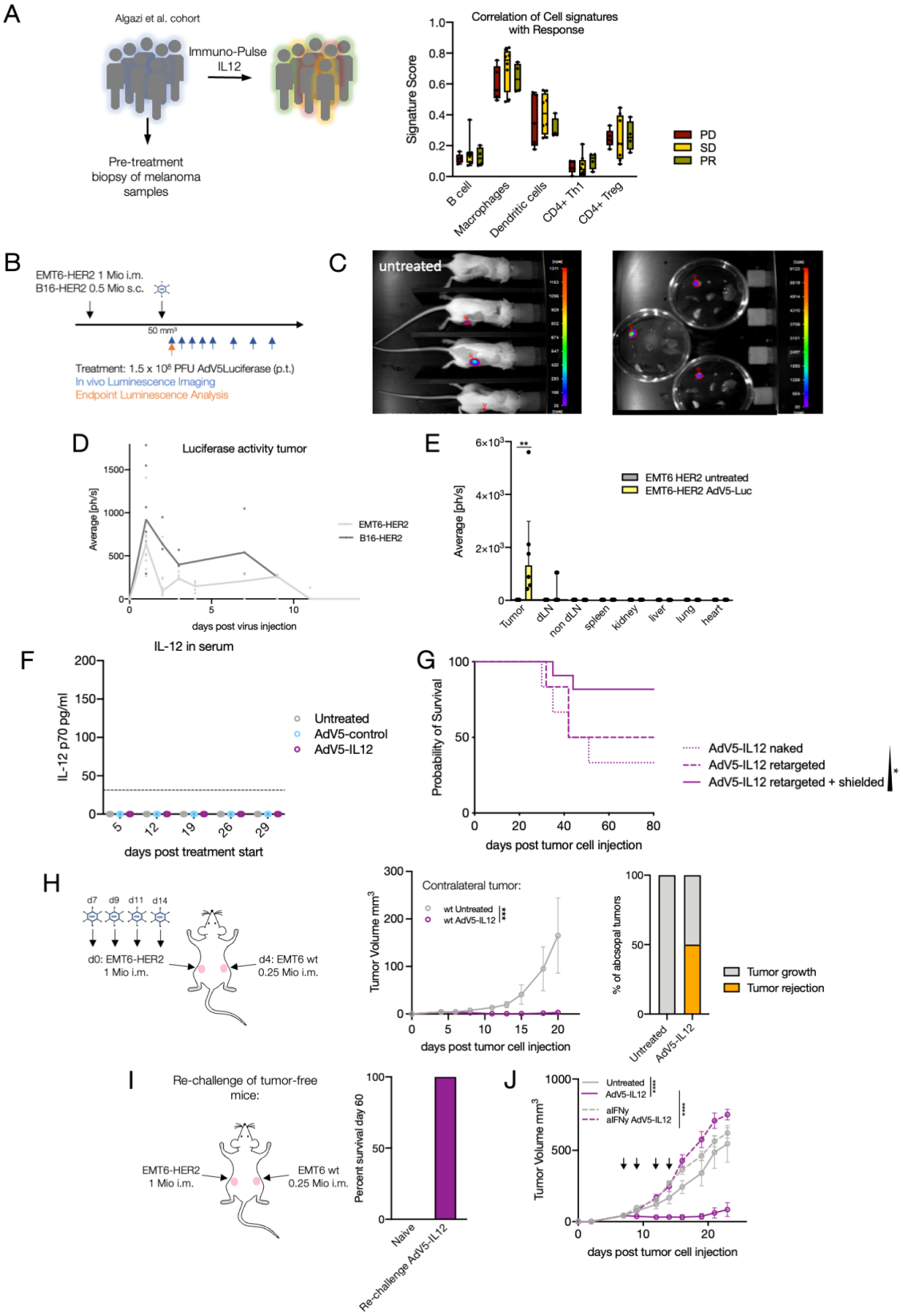

Fig. S1: Features of local IL-12 therapy.

(A) Cell signature scores measured by Nanostring in skin tumor biopsies from 19 patients with melanoma before intra-tumoral treatment with ImmunoPulse IL-12 were correlated with clinical response (PD:

progressive disease, SD: stable disease, PR: partial response) (**B)** Wildtype (WT) mice were engrafted with 1 mio EMT6-HER2 (i.m.) or 0.5 mio B16-HER2 (s.c.). Mice were p.t. treated with AdV5-Luciferase on day 7 or day 11 (tumor size 30–70 mm^3), respectively. The luciferase signal was live imaged at the indicated time points (blue arrows; day 1, 2, 3, 4, 5, 7, 9, 11 and 13 post virus injection). *n*= 6 mice per condition. (C) Representative luciferase signal in three treated and one untreated animal one day post AdV5-Luciferase injection are shown. After isolation of tumor, draining lymph node, non-draining lymph node, spleen, kidney, liver, heart and lung, luciferase signal was measured again. (**D)** Quantification of in vivo luciferase signal in EMT6-HER2 (light grey) and B16-HER2 (dark grey) tumors. (E) Quantification of luciferase signal one day post AdV5-Luciferase treatment in isolated indicated organs of EMT6-HER2 bearing mice. (**F)** Wildtype (WT) mice were engrafted with 1 mio EMT6-HER2 intramammarily (i.m.). From day 7 (tumor size 30–70 mm^3), mice were treated with $1.5x10^8$ PFU of HER2-targeted and shielded adenoviral vectors (peritumorally) encoding for IL-12 or empty control cassette (AdV5-control) on day 7, 9, 11 and 14. On the indicated days, serum was collected and IL-12 concentration was determined by ELISA. Dotted line denotes detection limit of the ELISA. (**G)** Wildtype (WT) mice were engrafted with 1 mio EMT6-HER2 intramammarily (i.m.). From day 7 (tumor size 30–70 mm^3), mice were treated with $1.5x10^8$ PFU of naked, HER2-targeted or HER2-targeted and shielded adenoviral vectors (peritumorally, p.t.) encoding for IL-12 or an empty control cassette (AdV5-control) on days 7, 9, 11 and 14 p.t. Kaplan-Meier survival curves are shown. Black arrows denote days of treatment. n = 6. Log rank test for trend was performed to determine significant changes. (**H)** Wildtype (WT) mice were engrafted with 1 mio EMT6-HER2 (i.m.) and with 4 days delay with 0.25 mio EMT6 wt cells on the contralateral flank. EMT6-HER2 tumors were peritumorally treated with AdV5-IL12. Tumor growth of contralateral tumor (EMT6 wt) was measured. Tumor growth curve and percentage of rejected contralateral tumors are shown. n = 6 mice per group. (**I)** Mice which rejected tumors after AdV5-IL12 treatment were rechallenged (60d after tumor rejection) with 1 mio EMT6-HER2 i.m. and 0.25 mio EMT6 wt cells (no HER2 transgene) on each flank. Percentage of survival 60d post rechallenge is shown. n = 12, naive mice served as a control. (**J)** Wildtype (WT) mice were engrafted with 1 mio EMT6-HER2 intramammarily (i.m.). From day 7 (tumor size 30–70 mm^3), mice were treated with $1.5x10^8$ PFU of HER2-targeted and shielded adenoviral vectors (peritumorally) encoding for IL-12 on day 7, 9, 11 and 14. IFNγ neutralization was performed using anti-IFNγ antibody injected every 2-3 days starting one day before virus inoculation. Tumor growth curves are shown. n = 5-6 mice. *P < 0.05, ** P < 0.01, *** P < 0.001, **** P < 0.0001. Error bar values represent SD or SEM (tumor growth curves). For comparisons between three or more groups, one-way ANOVA with multiple comparisons was used. For survival analysis, P values were computed using the Log Rank test. Two-way ANOVA was used to compare tumor growth curves.

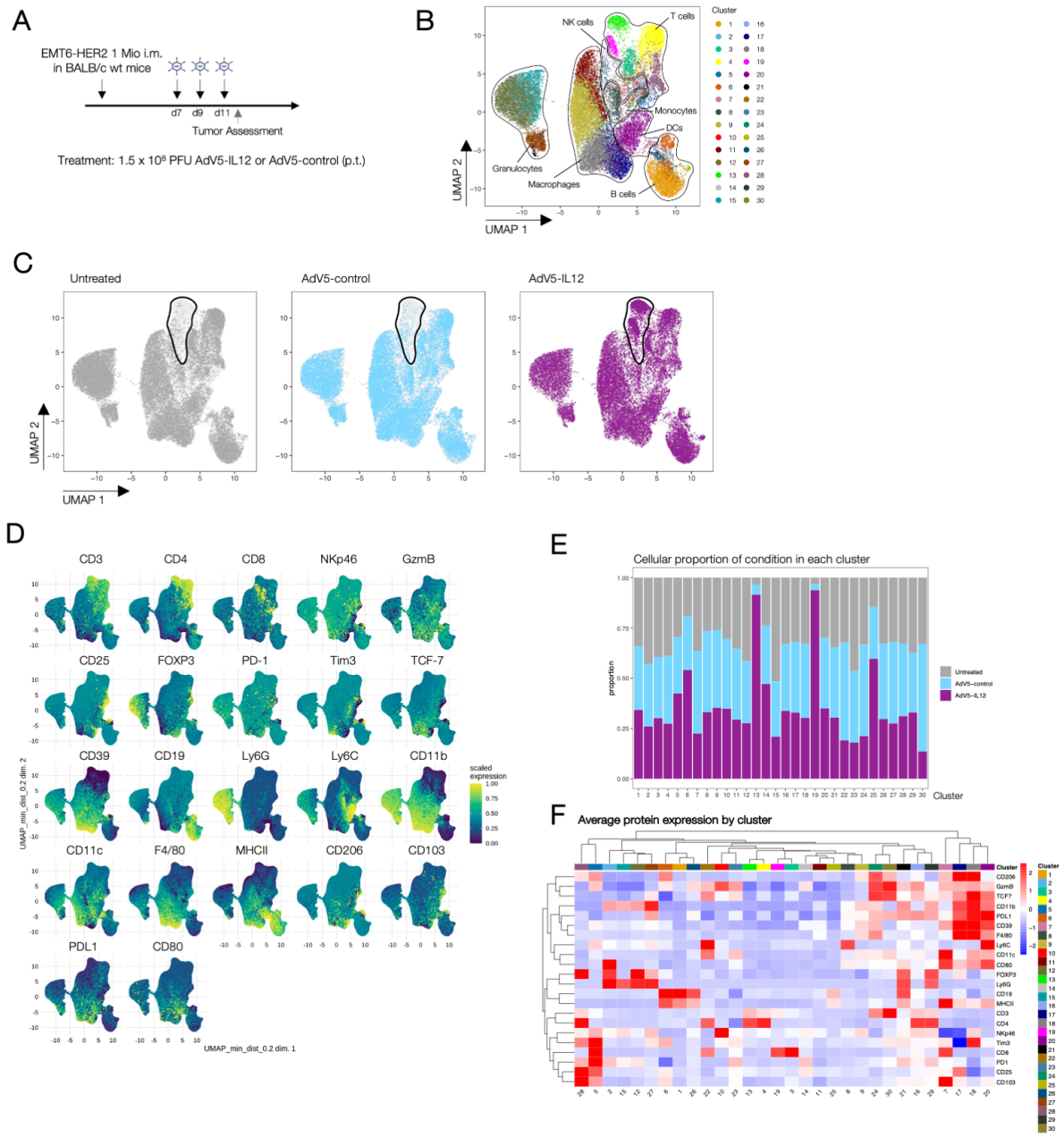

Fig. S2: Cellular composition after AdV5-IL12 therapy.

(A) Wildtype (WT) mice were engrafted with 1 mio EMT6-HER2 intramammarily (i.m.). Starting from day 7 (tumor size 30–70 mm^3), mice were treated with $1.5x10^8$ PFU of HER2-targeted and shielded adenoviral vectors (p.t.) encoding for IL-12 or empty control cassette (AdV5-control) on day 7, 9 and 11. On day 12 post inoculation, tumors were isolated and single cell suspensions were analyzed by flow cytometry. (**B)** UMAP projection is depicting the alive CD45+ tumor infiltrating lymphocytes colored by cluster. (**C)** UMAP projection is showing distribution of cells colored by treatment condition (dark grey: untreated; blue: AdV5-control; magenta: AdV5-IL12). (**D)** UMAP-projection of pooled conditions showing expression analyzed proteins supporting cell-type assignments. (**E)** Percentage of cells in each cluster by treatment. (**F)** Heatmap showing protein expression of 2 x 10^4 random cells assigned to conditions (Untreated, AdV5-control or AdV5-IL12) and cluster. *n* = 5-6 mice per group.

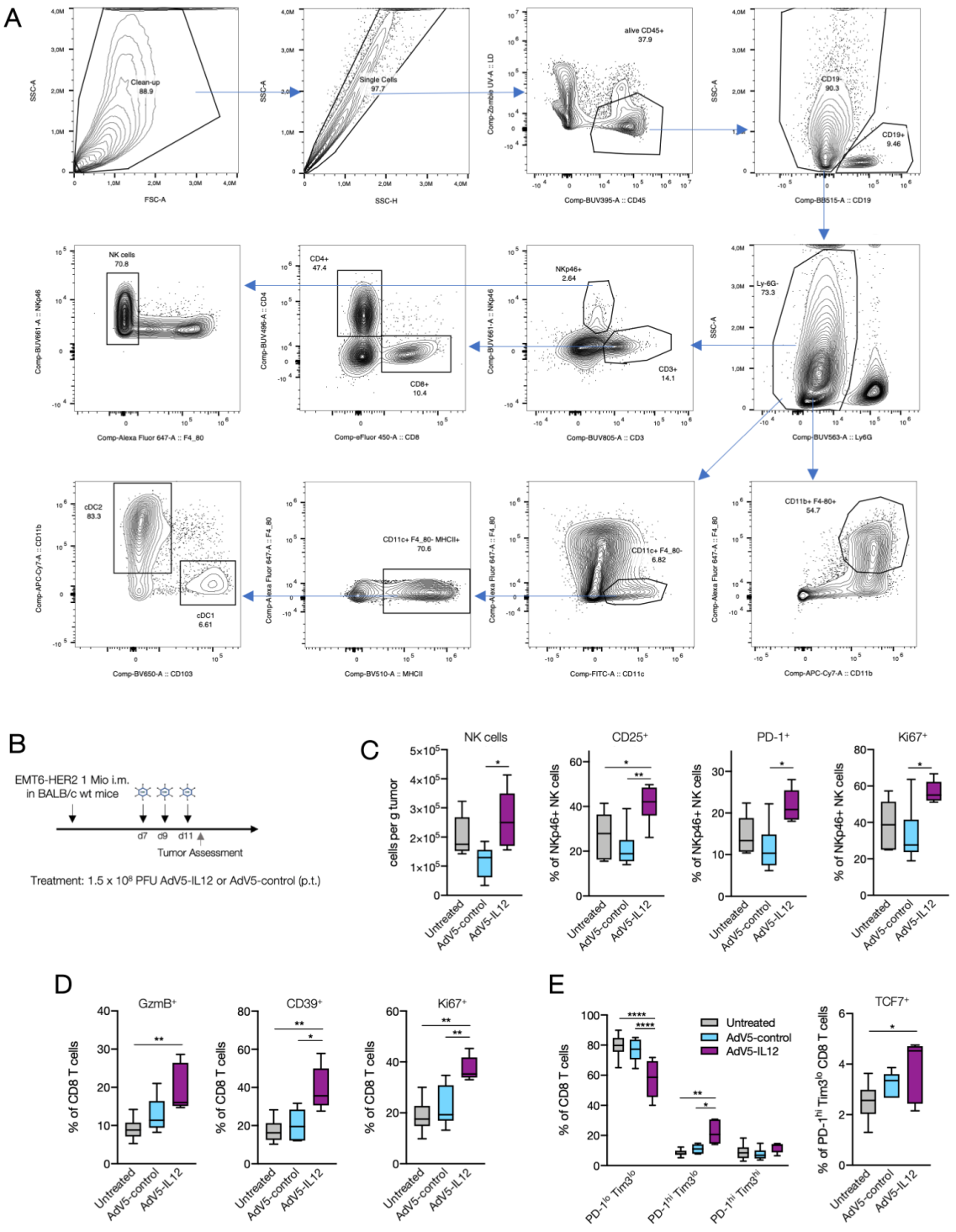

Fig. S3: Gating strategy and cellular changes after AdV5-IL12 therapy.

(A) To gate on singlets, SSC-A and SSC-H were used. After gating on alive CD45+ cells, CD19+ B cells and Ly-6G+ Granulocytes were excluded. To define T cells (CD3+), NK cells were excluded (NKp46+ F4/80-) and further distinguished between CD8 T cells and CD4 T cells. Macrophages were defined using F4/80+ and CD11b+. DCs were defined as CD11c+ F4/80- cells. MHCII was used to gate on cDCs. Subsequently to distinguish cDC1s from cDC2s, CD11b and CD103 was used. (**B)** Wildtype (WT) mice were engrafted with 1 mio EMT6-HER2 intramammarily (i.m.). Starting from day 7 (tumor size 30–70 mm^3),

mice were treated with $1.5x10^8$ PFU of HER2-targeted and shielded adenoviral vectors (p.t.) encoding for IL-12 or empty control cassette (AdV5-control) on day 7, 9 and 11. On day 12 post inoculation, tumors were isolated and single cell suspensions were analyzed by flow cytometry. (**C**) Quantification of NK cells (NKp46+, CD3-, Ly6G-, CD19-, F4/80-) per gram tumor and proportion of CD25+, PD-1+ or Ki67+ of NK cells between the different treatment conditions. (**D**) Proportion of granzyme B+ (GzmB+), CD39+ or Ki67+ of CD8 T cells (CD3+, CD4-, NKp46-, CD19-) between the different treatment conditions. (**E**) Proportion of PD-1^{lo}TIM3^{lo}, PD-1^{hi}TIM3^{lo} or PD-1^{hi}TIM3^{hi} intra-tumoral CD8 T cells in each treatment group. n = 5-6 mice per group. *$P < 0.05$, ** $P < 0.01$, *** $P < 0.001$, **** $P < 0.0001$. Error bar values represent SD. For comparisons between three or more groups, one-way ANOVA with multiple comparisons was used.

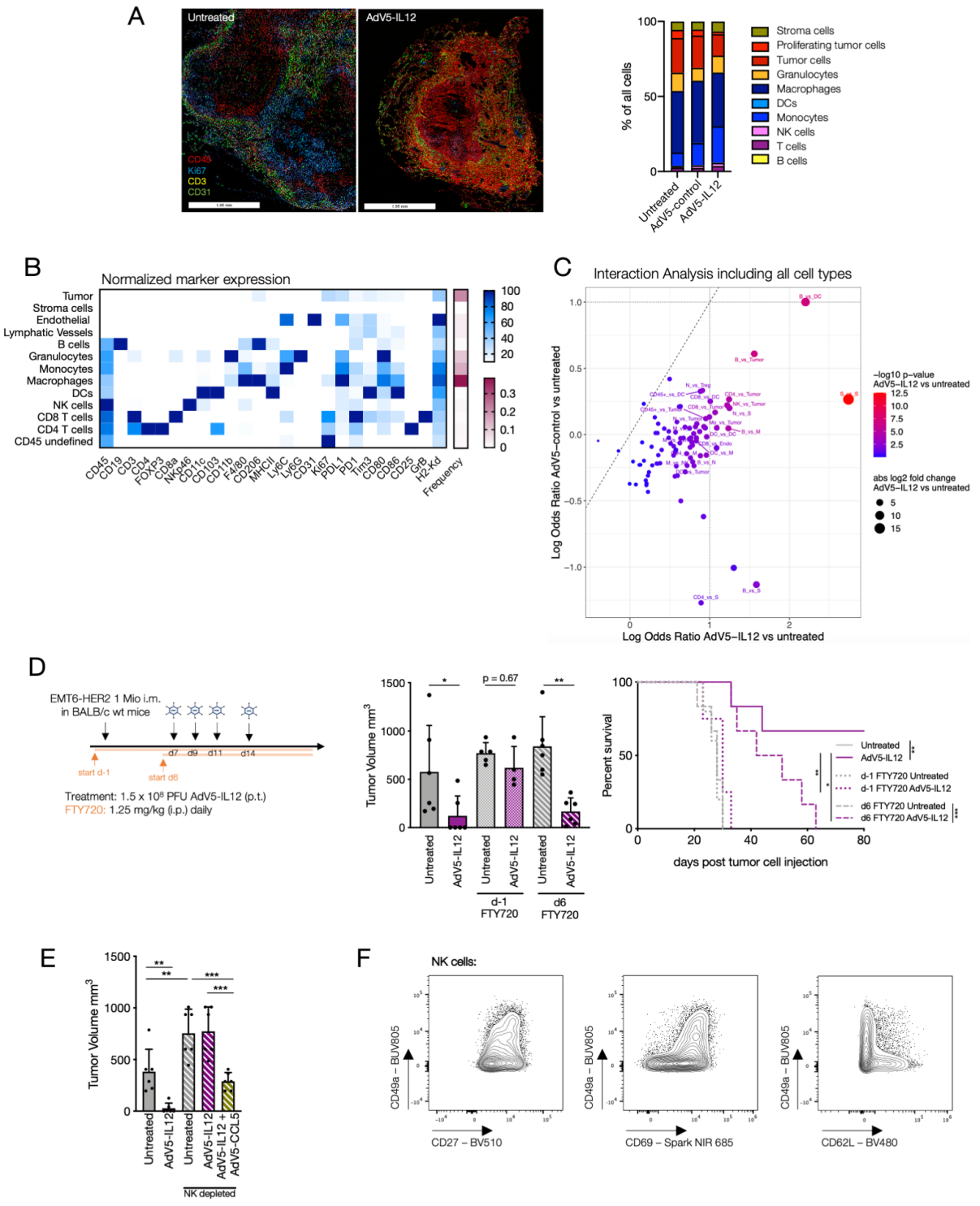

Fig. S4: Interaction analysis and functions of NK cells in efficacy of AdV5-IL12 treatment.

(A–B) Wildtype (WT) mice were engrafted with 1 mio EMT6-HER2 intramammarily (i.m.). Starting from day 7 (tumor size 30–70 mm^3), mice were treated with $1.5x10^8$ PFU of HER2-targeted and shielded adenoviral vectors (peritumorally) encoding for IL-12 or empty control cassette (AdV5-control) on day 7, 9 and 11. On day 12 post inoculation, tumors were isolated, embedded in OCT and analyzed by multiparameter immuno-fluorescence microscopy. *n*= 3 mice per condition. (**A)** Representative IF pictures are showing untreated and AdV5-IL12 treated tumors (CD45: red, Ki67: blue, CD3: yellow, CD31: green) including

quantification of main clusters between conditions. (**B)** Heatmap showing normalized marker expression and frequency of identified main populations. (**C)** Visualization of log odds ratios and *P* values for changes in all cell-cell type interactions between experimental conditions. (**D)** 1 mio EMT6-HER2 cells were injected in WT mice (i.m.). Starting from day 7 (tumor size 30–70 mm^3), mice were treated with $1.5x10^8$ PFU of HER2-targeted and shielded adenoviral vectors (peritumorally) encoding for IL-12 on day 7, 9, 11 and 14. Lymphocyte trafficking was inhibited using FTY720 as indicated (orange arrow and line). Tumor volume on day 23 post tumor inoculation and Kaplan-Meier survival curves are shown. (**E)** EMT6-HER2-engrafted mice were treated with AdV5-IL12 and AdV5-CCL5. Starting one day prior adenoviral therapy, NK cells were depleted using anti-AsialoGM1 antibody. Tumor volume on day 23 post tumor inoculation is shown. (**F)** Protein expression on intratumoral NK cells analyzed by flow cytometry of AdV5-IL12 treated EMT6-HER2-bearing mice. * $P < 0.05$, ** $P < 0.01$, *** $P < 0.001$, **** $P < 0.0001$. Error bar values represent SEM. For survival analysis, *P* values were computed using the Log Rank test. For comparisons between three or more groups, one-way ANOVA with multiple comparisons was used.

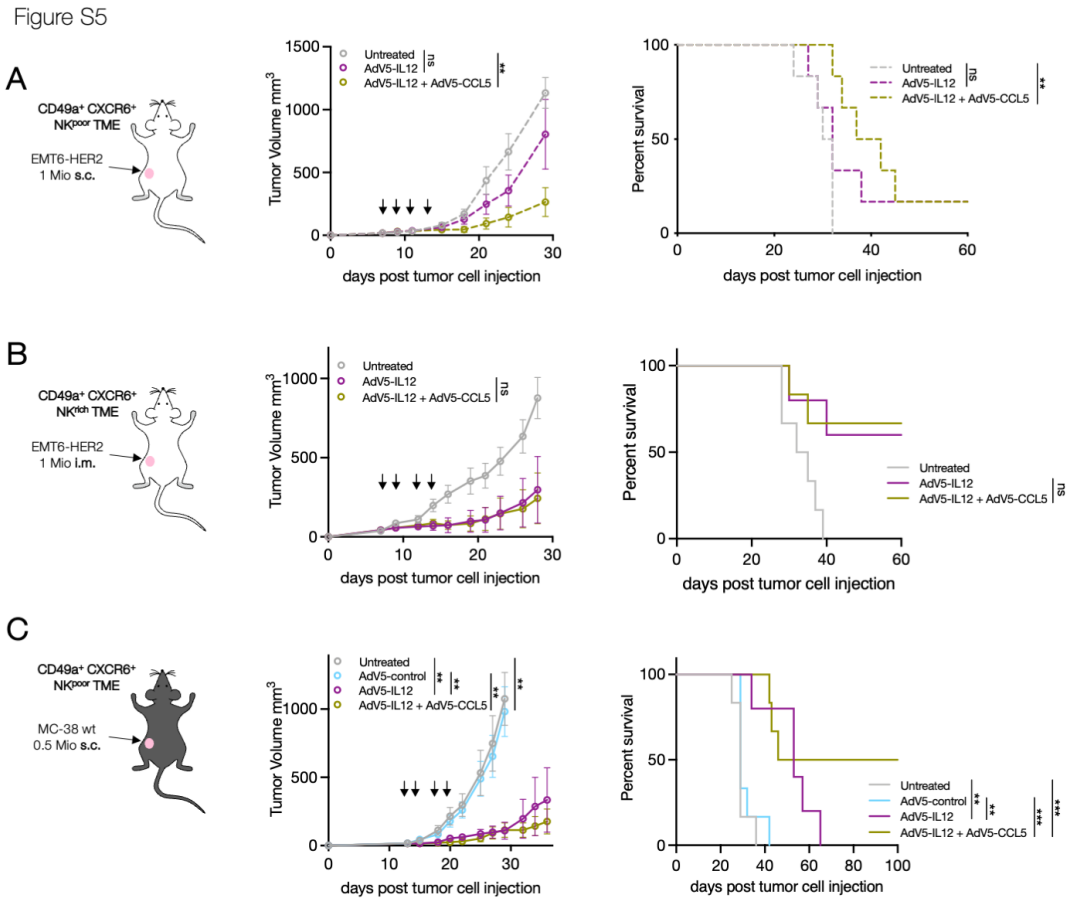

Fig. S5: AdV5-IL12 and AdV5-CCL5 efficacy in CD49a$^+$ CXCR6$^+$ **NK rich and poor tumor mouse models.** **(A–B)** WT mice were engrafted with 1 mio EMT6-HER2 s.c. (**A**) or i.m. (**B**). From day 7 (tumor size 30–70 mm^3), mice were treated with 1.5x10^8 PFU of HER2-targeted and shielded adenoviral vectors (peritumorally, p.t.) encoding for IL-12 alone or in combination with AdV5-CCL5 on days 7, 9, 11 and 14 p.t. Tumor growth curves and Kaplan-Meier survival curves are shown. (**C)** Mice were engrafted with MC-38 wt cell (s.c.) treated with shielded AdV5-control, AdV5-IL12 and AdV5-CCL5 on day 11, 13, 15 and 18 (tumor size 30–70 mm^3) after tumor inoculation as indicated. Tumor growth and Kaplan-Meier survival curves are shown. * $P < 0.05$, ** $P < 0.01$, *** $P < 0.001$, **** $P < 0.0001$. Error bar values represent SEM. For survival analysis, P values were computed using the Log Rank test. Two-way ANOVA was used to compare tumor growth curves. $n = 6$ mice per group.

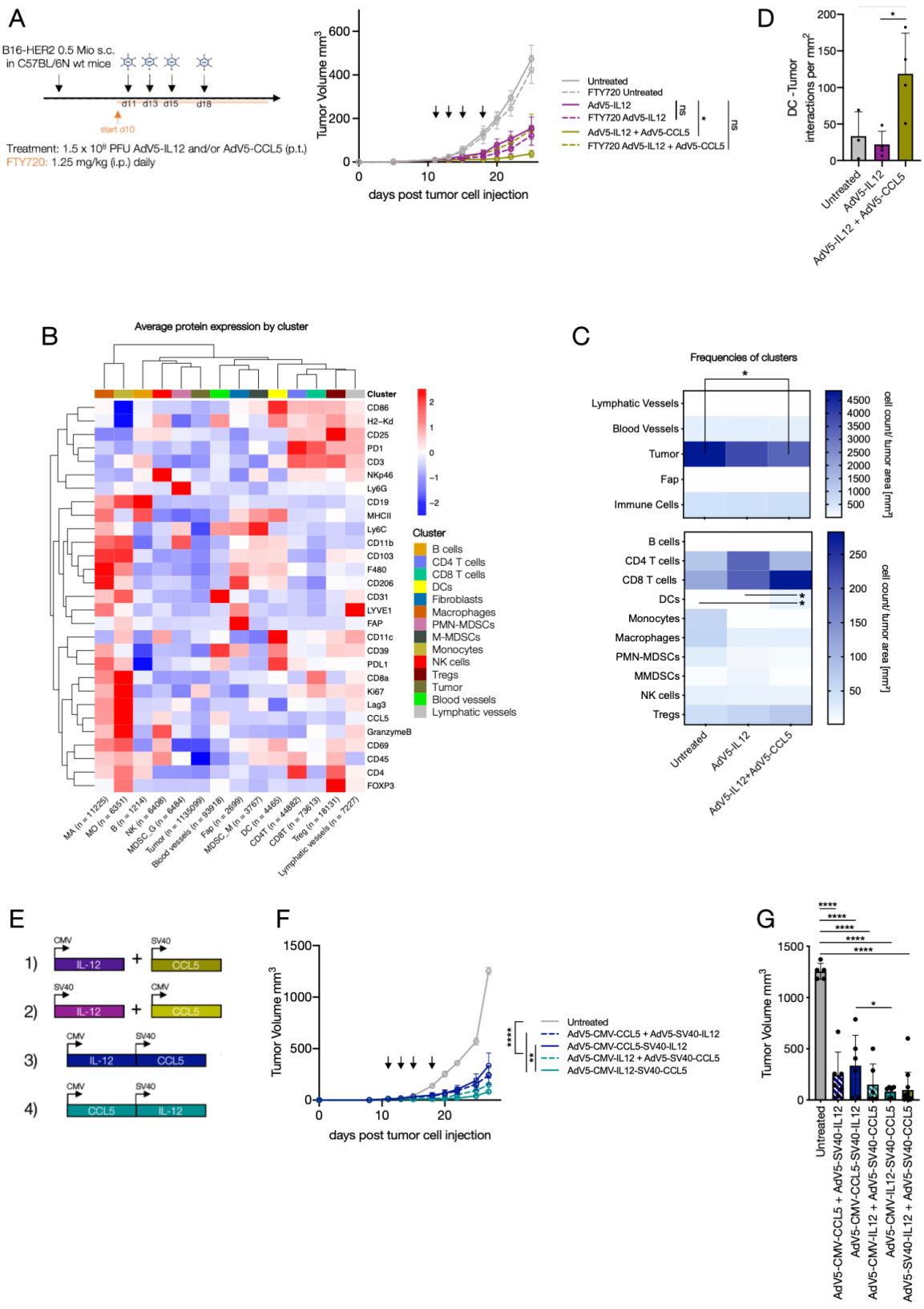

Fig. S6: Features of AdV5-IL12 and AdV5-CCL5 combinatorial therapy.

(A) Mice were treated with AdV5-IL12 and AdV5-CCL5 on day 11, 13, 15 and 18 (tumor size 30–70 mm^3) after B16-HER2 inoculation. Lymphocyte trafficking was inhibited using FTY720 as indicated (orange arrow and line). Tumor growth curves are shown. *n* = 5-6 mice per condition. Black arrows denote days of

treatment. (**B)** Wildtype (WT) mice were engrafted with 0.5 Mio B16-HER2 (s.c.). Starting from day 11 (tumor size 30–70 mm^3), mice were treated with $1.5x10^8$ PFU of HER2-targeted and shielded adenoviral vectors (p.t.) encoding for IL-12 and CCL5 on day 11, 13 and 15. On day 16 post inoculation, tumors were isolated, embedded in OCT and analyzed by multiparameter immuno-fluorescence microscopy. Heatmap showing normalized marker expression and (**C**) frequency of identified main populations. (**D)** Interaction count per mm^2 of tumor cells in close proximity to DCs. (**E)** Design of combinatorial vectors compared to mixture of single viruses. (**F)** Mice were treated with each $1.5x10^8$ PFU AdV5-IL12 and AdV5-CCL5 or $1.5x10^8$ PFU combinatorial vectors on day 11, 13, 15 and 18 (tumor size 30–70 mm^3) after B16-HER2 inoculation as indicated (black arrows). n = 5-6 mice per condition. Tumor growth curves are shown. (**G)** Quantification of tumor volume on day 27 post tumor inoculation. *$P < 0.05$, ** $P < 0.01$, *** $P < 0.001$, **** $P < 0.0001$. Error bar values represent SD or SEM (tumor growth curves). For comparisons between three or more groups, one-way ANOVA with multiple comparisons was used. Two-way ANOVA was used to compare tumor growth curves.

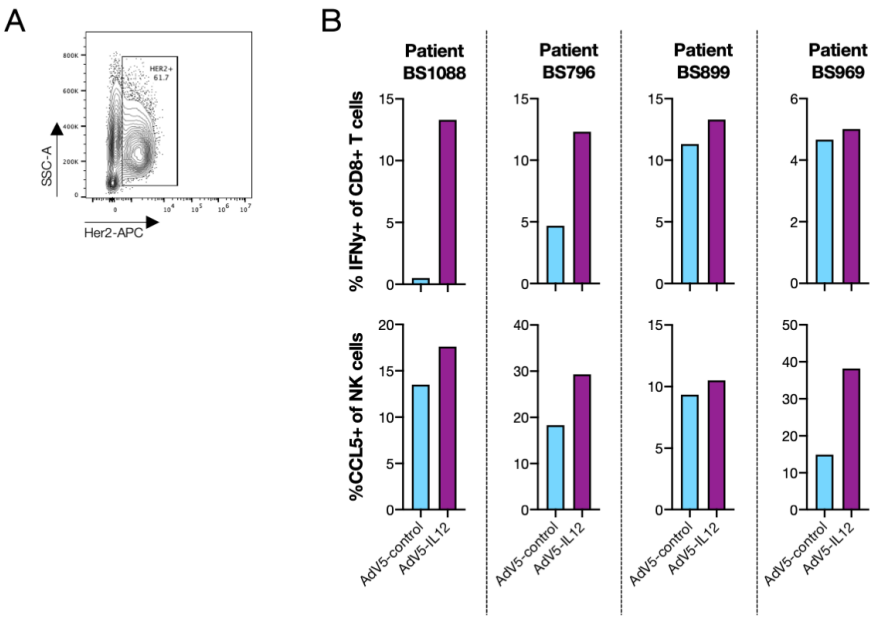

Fig. S7: CCL5 and IFNγ expression in primary human tumor fragments after AdV5-IL12 treatment.

HER2+ ovarian cancer samples were dissected into tumor fragments and cultivated embedded in matrigel. Tumor fragments were treated with HER2-targeted AdV5 encoding human IL-12 for 48 h (8-12 fragments per condition). (**A)** Representative dot plot of HER2 expression analyzed by flow cytometry. (**B)** After treatment tumor fragments per condition were pooled and analyzed by flow cytometry. Quantification of IFNγ+ CD8 T cells (CD3+, CD56-) and NK cells (CD56+, CD3-) after treatment.

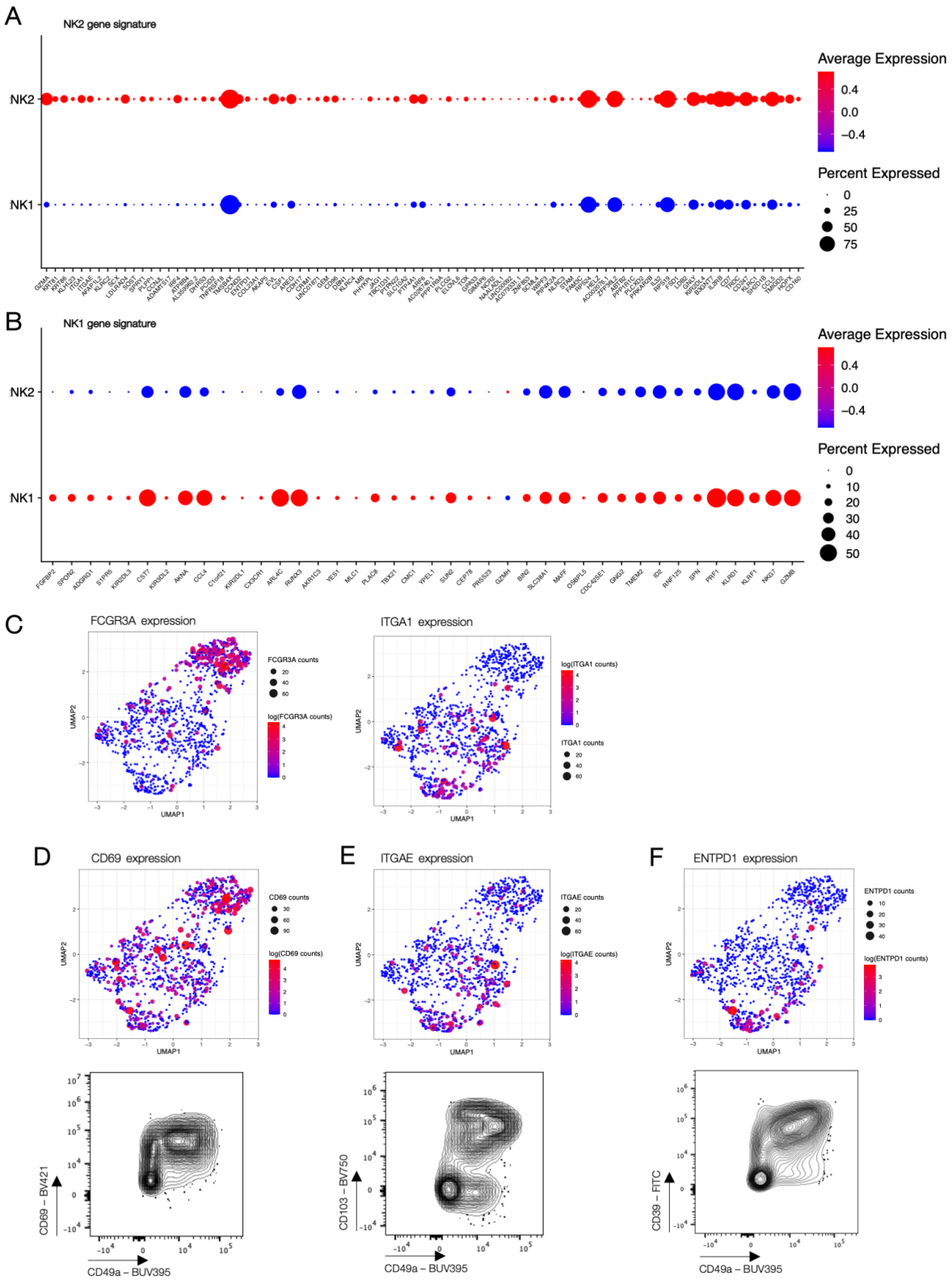

Fig. S8: Gene and protein expression of intratumoral NK cells.

(A–B) Dotplot to visualize expression of genes in tumor-infiltrating NK cells of patients with NSCLC defining generated (**A**) NK2 and (**B**)NK1 signature is shown. (**C**) *FCGR3A* and *ITGA1* expression is visualized on UMAP projection of tumor-infiltrating NK cells of patients with NSCLC. (**D–F**) Comparison of gene

expression of scRNASeq data set of tumor-infiltrating NK cells to protein expression analyzed by flow cytometry of patients with NSCLC (**D**) CD69, (**E**) *IGTAE*/CD103, (**F**)*ENTPD1*/CD39).

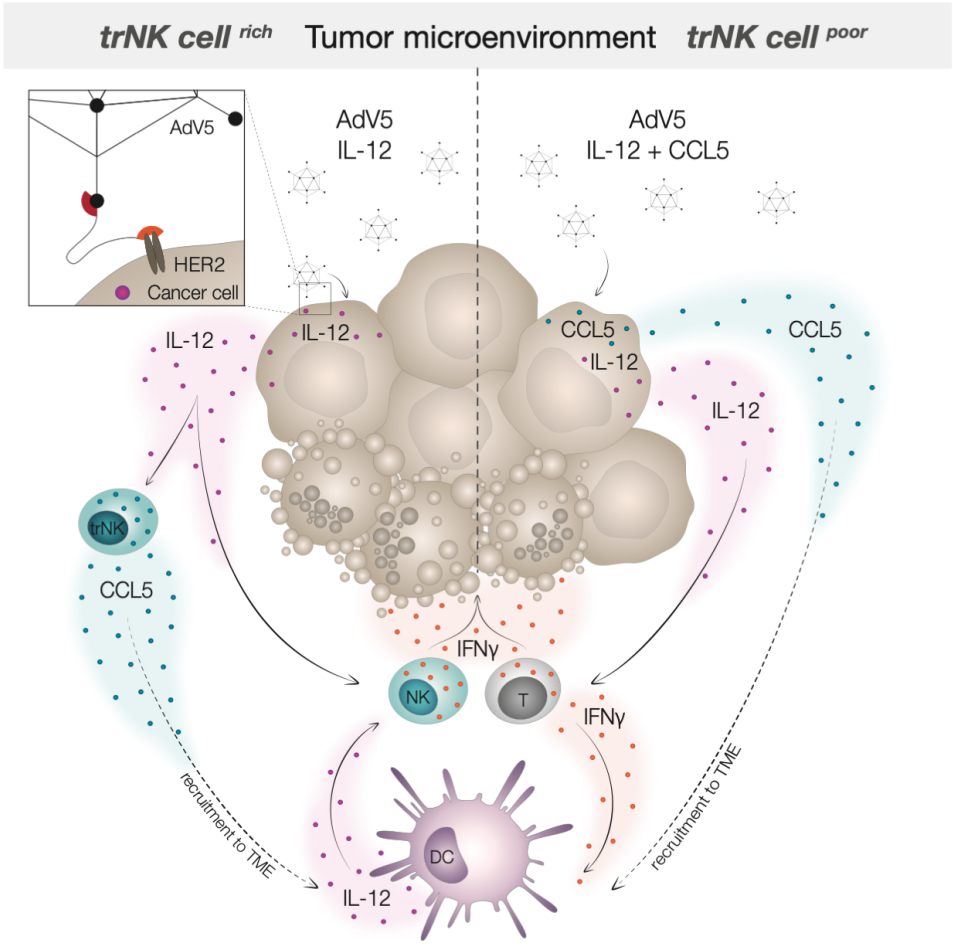

Fig. S9: Graphical abstract. In TME with high amount of NK cells with tissue-resident traits (left panel; trNK cell ^{rich}), AdV5-IL12 imposes expression of the DC-attractant CCL5, inducing T cell immunity. Failure to respond to IL-12 in tumor models with low CD49a^{+} CXCR6^{+} NK cell infiltration (right panel; trNK cell ^{poor}) could be overcome by intra-tumoral delivery of CCL5.

Table S1: Flow cytometry antibodies.

Fluorophore	Antigen	Clone	Supplier	Cat#
PE	CCL5	VL1	BioLegend	515504
PE	CCL5	2E9/CCL5	BioLegend	149104
PE-Cy7	CCL5	2E9/CCL5	BioLegend	149105
BV570	CCR5	C34-3448	BD Biosciences	746501
BV650	CD103	2E7	BD Biosciences	748256
BV750	CD103	BER-ACT8	BD Biosciences	747099
APC-Cy7	CD11b	M1/70	BioLegend	101226
FITC	CD11c	N418	BioLegend	117306
Pac Blue	CD14	M5E2	BioLegend	301828
BUV496	CD16	3GA	BD Bioscience	612945
BB515	CD19	1D3	BD Biosciences	564509
FITC	CD19	1D3	BD Biosciences	553785
BV711	CD206	C068C2	BioLegend	141727
PE-Cy5.5	CD25	PC61.5	Thermo Fisher Scientific	35-0251-82
BV510	CD27	LG.3A10	BioLegend	124229
APC-H7	CD3	SK7	BD Biosciences	560275
BUV805	CD3	145-2C11	BD Biosciences	741895
BUV805	CD3	UCHT-1	BD Bioscience	612896
BV605	CD3	SK7	BioLegend	344836
PE-Dazzle594	CD3	17A2	BioLegend	100246
FITC	CD39	A1	BioLegend	328206
PE	CD39	24DMS1	Thermo Fisher Scientific	eBio 12-0391-82
BUV496	CD4	GK1.5	BD Biosciences	612952
AF532	CD45	HI30	Thermo Fisher Scientific	58-0459-41
BUV395	CD45	30-F11	BD Biosciences	564279
PerCP-Cy5.5	CD45	2D1	Thermo Fisher Scientific	9045-9459-120
BUV395	CD49a	SR84	BD Bioscience	742363
BUV805	CD49a	Ha31/8	BD Biosciences	741976
BUV661	CD56	NCAM16	BD Biosciences	750478
BV785	CD56	5.1H11	BioLegend	362550
BV480	CD62L	MEL-14	BD Biosciences	746726
BV421	CD69	FN50	BioLegend	310930
SparkNIR685	CD69	H1.2F3	BioLegend	104557
BUV805	CD8	RPA-T8	BD Biosciences	749366
eFluor 450	CD8	53-6.7	Thermo Fisher Scientific	eBio 48-0081-82
PE-Cy7	CD8	SK1	Thermo Fisher Scientific	9025-0087-120
BV605	CD80	16-10A1	BioLegend	104792

BUV737	CXCR3	CXCR3-173	BD Biosciences	741895
PerCp-Cy5.5	CXCR6	SA051D1	BioLegend	115111
AF647	F4/80	BM8	BioLegend	123122
FITC	F4/80	BM8	BioLegend	123108
APC	FoxP3	FJK-16s	Thermo Fisher Scientific	17-5773-82
PE-eFluor610	GzmB	NGZB	Thermo Fisher Scientific	61-8898-82
APC	IFNy	XMG1.2	BioLegend	505810
BB700	IFNy	B27	BD Biosciences	566395
FITC	IFNy	C4.B3	Thermo Fisher Scientific	11-7319-82
AF532	Ki67	SolA15	Thermo Fisher Scientific	58-5698-82
PerCP	Ly-6C	HK1.4	BioLegend	128028
BUV563	Ly-6G	1A8	BD Biosciences	612921
FITC	Ly6G	1A8	BD Biosciences	551460
BV510	MHCII I-A/I-E	M5/114.15.2	BioLegend	107636
FITC	MHCII I-A/I-E	M5/114.15.2	BioLegend	107606
BUV661	NKp46	29A14	BD Biosciences	741678
BV421	NKp46	29A1.4	BD Biosciences	562850
BV785	PD-1	29F.1A12	BioLegend	135225
BV421	PD-L1	10F.9G2	BioLegend	124315
AF700	TCF-7	# 812145	R&D Systems	FAB8224N
BB700	Tim-3	5D12/TIM-3	BD Biosciences	747619

Table S2: Microscopy antibodies.

Antigen	Clone	Supplier	Cat#
Granzyme B	GB11	invitrogen	MA1-80734
CXCL9	MIG-2F5.5	BioLegend	515602
CD40	1C10	BioLegend	102802
PD1	29F.1A12	BioLegend	135202
FOXP3	FJK-16s	eBioscience	14-5773-82
CD80	16-10A1	BioLegend	104702
IFNy	H22	BioLegend	513202
H-2Kd	34-1-2S	ThermoFisher	MA5-18008
Tim-3	RMT2-23	BioLegend	119702
NKp46	29A1.4	BioLegend	137602
CD25	PC61	BioLegend	102002
F4/80	BM8	BioLegend	123102
Ly-6C	HK1.4	BioLegend	128002
IL12	C15.6	BioLegend	505202
CD103	2.00E+07	BioLegend	121402
PD-L1	10F.9G2	BioLegend	124302
CD107a	1D4B	BioLegend	121602

CD206	C068C2	BioLegend	141702
CD11c	N418	Akoya	4350013
CD3	17A2	Akoya	4350014
Ly6G	1A8	Akoya	4350015
CD45	30-F11	Akoya	4150002
CD11b	M1/70	Akoya	4150015
CD31	MEC13.3	Akoya	4250001
CD44	IM7	Akoya	4250002
MHCII	M5/114.15.2	Akoya	4250003
CD19	6D5	Akoya	4250014
CD4	RM4-5	Akoya	4250016
CD8a	53-6.7	Akoya	4250017
Ki67	B56	Akoya	4250019